Optical properties and oxidative potential of aqueous-phase products from OH and ^{3}C*-initiated photolysis of eugenol

Xudong Li[1], Ye Tao[1], Longwei Zhu[1], Shuaishuai Ma[1], Shipeng Luo[1], Zhuzi Zhao[1], Ning Sun[1], Xinlei Ge[2,*], Zhaolian Ye[1,*]

[1]College of Chemistry and Environmental Engineering, Jiangsu University of Technology, Changzhou 213001, China

[2]Jiangsu Key Laboratory of Atmospheric Environment Monitoring and Pollution Control, Collaborative Innovation Center of Atmospheric Environment and Equipment Technology, School of Environmental Sciences and Engineering, Nanjing University of Information Science and Technology, Nanjing 210044, China

*Correspondence: Zhaolian Ye (bess_ye@jsut.edu.cn) and Xinlei Ge (caxinra@163.com)

Abstract: In ambient air, aqueous reactions may turn precursors into more light-absorbing and toxic products, leading to air quality deterioration and adverse health effects. In this study, we investigated eugenol degradation in the aqueous phase by direct photolysis, and indirect photo-oxidation under two radicals (triplet excited state (^{3}C*) and hydroxyl radical (•OH)). Results showed degradation rates of eugenol followed the order of ^{3}C*>•OH >direct photolysis. Relative contributions of reactive oxygen species (ROS) were evaluated via combination of radical quenching tests, deoxygenated experiments and ESP method, and results showed that ^{3}C* played a dominant role in eugenol degradation for ^{3}C*-initiated oxidation, while both O_2 and $O_2^{•-}$ generated were important for OH-initiated oxidation. Rate constants under O_2, air and

N2 followed the order of $k_{O_2} > k_{Air} > k_{N_2}$ for both direct photolysis and OH oxidation,

and it changed to $k_{Air} > k_{N_2} > k_{O_2}$ for $^3C^*$-initiated oxidation. Light absorption spectra

showed absorbance at 300-400 nm, and the intensity increased as photolysis

progressed, and there were new broad fluorescent spectra at excitation/emission

(Ex/Em)=250/(400-500) nm, suggesting the formation of new chromophores and

fluorophores, such as humic-like substances (HULIS). Additionally, distinct

fluorescence peaks appeared at Ex/Em=(300-350)/300 nm at different oxidation stages.

Concentration of generated HULIS increased gradually over time, then leveled off.

Dithiothreitol (DTT) assay was applied to assess oxidation potential of the products,

which was greater than that of parent eugenol, suggesting more harmful species were

produced during oxidation. Detailed reaction pathways were elucidated via analyses of

chemical characteristics of the products.

Keywords: Aqueous-phase reaction; reactive oxygen species (ROS); fluorescence

spectra, DTT method, oxidative potential

1 Introduction

Photochemical reactions in the atmospheric aqueous phase (cloud droplet, fog

droplet and aerosol water) affect the lifetimes of many organic species, and are

important sources and aging pathway of secondary organic aerosol (SOA) (Vione et al.,

2006; Zhao et al., 2012). Different from the gasSOA formed through gas-phase

photochemical oxidation, aqueous-phase SOA (aqSOA) typically are usually more

oxidized and lower volatile, so it plays an important role in haze formation, air quality

and global climate change (Ervens et al., 2011; Lim et al., 2010). However, due to

complicated underlying reaction mechanisms and control factors (such as precursors,

oxidants, radicals and light intensity), there are still many unknowns regarding the impacts of aqueous reactions. For example, reaction mechanism, optical property, oxidative potential (OP) and relations between them remain not yet poorly understood.

Most laboratory studies so far have focused on aqueous-phase oxidation of small molecular weight VOCs, such as isoprene, terpenes (α-pinene and β-pinene), as well as their gas-phase oxidation products (such as glyoxal, methylglyoxal, *cis*-pinonic acid and methyl vinyl ketone) (Faust et al., 2017; Huang et al., 2011; Lee et al., 2012; Zhang et al., 2010). Now concerns have been extended to semi-/intermediate volatility VOCs (S/IVOCs), especially phenolic compounds, which could be produced by combustion or pyrolysis of lignin in biomass (Gilardoni et al., 2016; He et al., 2019; Jiang et al., 2021; Li et al., 2014; Li et al, 2021; Mabato et al., 2022; Tang et al., 2020; Yang et al., 2021; Yu et al., 2016). Our group also has been studying aqueous-phase oxidation of phenolic compounds (Chen et al., 2020). Aside from influence of types of precursors, the role of radicals in aqSOA formation also cannot be neglected. It is evident that liquid water contains many oxidants, such as molecular oxygen (O_2), nitrate radical (NO_3), hydroxyl radical (•OH), and organic triplet excited states ($^3C^*$), which play important roles in photochemical oxidation reactions (Kaur and Anastasio, 2018; Scharko et al., 2014). Among them, •OH is the predominant oxidant in atmospheric cloud/fog droplet/aerosol water, with concentration of 10^{-13}-10^{-12} mol·L^{-1} (Arakaki et al., 2013; Gligorovski et al., 2015; Herrmann et al., 2003). Hence, aqueous phase •OH-induced photodegradation has been extensively studied (Sun et al., 2010; Yu et al., 2016; Chen et al., 2020). Compared to •OH oxidation, $^3C^*$-initiated aqueous phase reaction (photosensitized reaction) has also attracted attention in the past years. Several classes of organic compounds in the atmosphere, including non-phenolic aromatic carbonyls, quinones, aromatic ketones and nitrogen-containing heterocyclic compounds, can form

74 $^3C^*$ after absorbing light (Alegría et al., 1999; Kaur et al., 2019; Nau and Scaiano, 1996;

75 Rossignol et al., 2014). These compounds are called photosensitizers. $^3C^*$ is capable of

76 reacting with O_2 to produce singlet oxygen ($^1O_2$) and superoxide radicals ($O_2^{\cdot-}$). Various

77 reactive oxygen species (ROS) can be generated and play a critical role in $^3C^*$-initiated

78 aqueous-phase reactions. Despite strong evidence in support of the importance of ROS

79 in photochemical process (Wu et al., 2021), however, our understanding on SOA from

80 $^3C^*$-initiated reaction is still limited, and contribution of possible ROS species has never

81 been clearly demonstrated.

82   Excitation-emission matrix (EEM) fluorescent spectroscopy, as a low-cost, rapid,

83 non-destructive and high-sensitivity technique, can offer detailed information on

84 chromophores hence has been widely employed for studies of aquatic dissolved organic

85 matter (Aryal et al., 2015). However, it has not been extensively used in atmospheric

86 aerosol research (Mladenov et al., 2011). Several recent studies have investigated the

87 relationship between the fluorescence components and chemical structures of

88 atmospheric aerosols through combining high-resolution aerosol mass spectrometry

89 (AMS) and EEM fluorescent spectroscopy (Chen et al., 2016a; Chen et al., 2016b).

90 Earlier report from Chang and Thompson (2010) found fluorescence spectra of reaction

91 products during aqueous reaction of phenolic compounds, with some similarities with

92 aerosol Humic-like substances (HULIS); Tang et al.(2020) also observed light-

93 absorbing products formed in aqueous-phase OH oxidation of vanillic acid and further

94 verified that aqueous reaction was a potential source of HULIS. Recently, Li et al. (2021)

95 began to apply EEM technique to characterize formation of light-absorbing compounds

96 in aqueous-phase oxidation of syringic acid. Additionally, studies (Chang and

97 Thompson, 2010) showed that light-absorbing and fluorescent substances generally

98 have large conjugated moieties (i.e., quinones, HULIS, polycyclic aromatic

99   hydrocarbons (PAHs)), which can damage human body (Dou et al., 2015; McWhinney

100 et al., 2013). HULIS are considered as an important contributor to induce oxidative

101 stress since they can served as electron carriers to catalyze ROS formation.

102 Dithiothreitol (DTT) assay (Alam et al., 2013; Chen et al., 2021; Verma et al., 2015a),

103 as a non-cellular method, was widely employed to determine oxidation activity and

104 assess oxidative potential of atmospheric PM via the rate of DTT consumption (Chen

105 et al., 2019; Cho et al., 2005), since oxidative stress was related to adverse health effect.

106 Some other works (Fang et al., 2016; McWhinney et al., 2013; Verma et al., 2015)

107 focused on the link between chemical composition and OP in PM, and has confirmed

108 that several kinds of compounds, such as quinones, HULIS and transition metals

109 usually have strong DTT activities. However, to the best of our knowledge, DTT

110 method has not been applied to evaluate the OP of aqueous-phase oxidation products

111 up to now.

112 In the present work, we choose eugenol as a model compound to conduct aqueous

113 phase reaction. Eugenol is a representative IVOC with moderate water-solubility (2.46

114 g/L at 25°C). We compared the product properties under direct photolysis (without

115 oxidant) and photo-oxidation upon two radicals (•OH and $^3C^*$). The characteristics of

116 products were statistically elucidated by combining results from high-performance

117 liquid chromatography (HPLC), ultraviolet and visible (UV-Vis) spectrophotometry,

118 gas chromatography mass spectrometry (GC-MS), EEM and soot-particle aerosol mass

119 spectrometer (SP-AMS). The relative importance of various ROS species to eugenol

120 degradation was explored, which was helpful for deeply clarifying the degradation

121 mechanism. This study also investigated the light-absorption, fluorescent and oxidative

122 properties of the aqueous oxidation products.

123 **2 Materials and methods**

2.1 Chemicals and reagents

Eugenol (99%), tert-butanol (TBA, 99%), 3,4-dimethoxybenzaldehyde (DMB, 99%), para-benzoquinone (*p*-BQ, 99%), dithiothreitol (99%) and 5,5′-dithiobis-2-nitrobenzoic acid (DTNB, 99%), 2-nitro-5-thiobenzoic (99%) and 2,2,6,6-tetramethylpiperidine(TEMP) were all purchased from Sigma-Aldrich chemical company. Superoxide dismutase (SOD) was from Bovine Erythrocytes BioChemika. Dichloromethane (HPLC-MS grade, 99%), methanol (HPLC-MS grade, 99%), acetonitrile (HPLC-MS grade, 98%), H_2O_2 (35 wt. %), and 2,4,6-trimethylphenol (TMP, 99%) were all obtained from Acors Chemicals. Sodium azide (NaN_3, 98%) was purchased from J&K Scientific Ltd. (Beijing, China). All solutions were prepared using ultrapure water (Millipore) on the day of experiments.

2.2 Photochemical experiment

Aqueous phase photochemical reactions were carried out in a Rayonet photoreactor (model RPR-200), equipped with 16 light tubes (equipped with 2 RPR-3000, 7 RPR-3500 and 7 RPR-4190), which was frequently used for photochemical reaction and described in detail by several groups (George et al., 2015; Hong et al., 2015; Huang et al., 2018; Jiang et al., 2021; Zhao et al., 2014) to mimic sunlight. Pyrex tubes containing sample solution were placed in the central and received radiation from surrounded lamps from all sides. At the bottom of sample tubes, there are fan and magnetic stir bar to make solution full mixed and maintain solution temperature of 25 ±2°C. The photoreactor system was the same as above mentioned and normalized distribution of the photon fluxes inside RPR-200 illumination system have been reported elsewhere (George et al., 2015). According to their description, the wavelength

of photon fluxes was over 280 and 500 nm range. In this work, we only measured light intensity at the surface of the reaction solution with a radiometer (Photoelectric instrument factory of Everfine Corporation, Hangzhou, China). The light intensity in the range of 290-320 nm (UVB) was ~2400 $\mu W/cm^2$, which was slightly lower than sunlight intensity (6257.1 $\mu W/cm^2$).

In this work, 300 μM H_2O_2 and 15 μM DMB were added into solution as sources of •OH and $^3C^*$ radicals, respectively. The initial concentrations of eugenol was applied as 300 μM. For $^3C^*$-mediated experiment, solutions were adjusted to pH=3 by H_2SO_4 in order to perform experiments under optimal conditions (Smith et al., 2014) since DMB triplet state is protonated to a more reactive form in acidic solutions. We conducted three sets of photolysis experiments: (A) 300 μM eugenol+300 μM H_2O_2; (B) 300 μM eugenol+15 μM DMB; and (C) 300 μM eugenol. In each series of photochemical oxidation, a darkness control experiments was done synchronously with a Pyrex tubes wrapped by aluminum foil. The control results showed the loss of eugenol under dark reaction could be negligible (data now shown). In addition, to evaluate the role of ROS to eugenol degradation in $^3C^*$-initiated oxidation process, quenching experiments using specific scavengers to trapping produced ROS were performed, such as TBA for •OH, NaN_3 for $^1O_2$, SOD for $O_2^{•-}$, and TMP for $^3C^*$, respectively (Pan et al., 2020; Wu et al., 2021). In •OH-initiated oxidation process, quenching experiments using p-BQ for $O_2^{•-}$ (Raja et al., 2005; Ma et al., 2019), and TBA for •OH were conducted. For most series of experiments, solution was saturated by air and all experiments presented were conducted in triplicate unless otherwise stated. The results were shown in respect of average plus/minus standard deviation. In order to further evaluate the role of oxygen in the photo-degradation, experiment were also conducted under different saturated gas (air, N_2 and O_2).

2.3 Analytical methods

2.3.1 Determination of eugenol concentration

Before and during the irradiation, 2 mL of reacted and controlled solutions were sampled periodically and subjected to HPLC (LC-10AT, Shimadzu, Japan) to quantify the eugenol concentrations. HPLC was equipped with the InertSustain AQ-C18 reverse phase column (4.6×250 mm, 5.0 μm, Shimadzu) and a UV-vis detector. The mobile phase was a mixture of acetonitrile/H_2O (v/v: 60/40) at a flow rate of 0.6 mL/min, and the detection wavelength was set at 280 nm. The kinetic rate constant of eugenol degradation can be obtained from the slope of plot of $-\ln(c_t/c_0)$ versus reaction time as presented in Eq.(1).

$$\ln(c_t/c_0) = -kt \tag{1}$$

Here,c_0 (μM) and c_t (μM) are eugenol concentration at the initial and reaction time t; k stands for pseudo first order rate constant.

2.3.2 UV-Vis and fluorescent spectra

The UV-Vis absorbance spectra of reacted solutions (placed in a quartz cuvette with a path length of 1 cm) were measured by using an UV-Vis spectrophotometer (Specord 210 plus, Analytik Jenal). The instrument is a dual-beam optical system with tungsten and deuterium lamps as light sources. A reference absorption spectrum of ultrapure water was carried out in the same cuvette prior to sample analysis for baseline correction.

Immediately following UV-Vis measurement, the cuvette was transferred to a three-dimensional EEM fluorescence spectrometer (FluoroMax Plus,HORIBA Scientific) to record variation of fluorescence intensity upon irradiation. Spectral ranges

195 varied from 200 to 450 nm for excitation wavelengths (Ex) and from 290-650 nm for

196 emission wavelength (Em). Excitation and emission wavelength intervals were 5 nm

197 and 2 nm steps, respectively. The reported absorbance and EEM spectra are the average

198 of the results from triplicate experiments.

199 2.3.3 Determination of HULIS concentration

200 Solid phase extraction (SPE) cartridge were used to isolate HULIS from the

201 reaction solution. The original SPE cartridges was rinsed with 1 mL ultrapure water and

202 3 mL methanol before extraction. The solution (25 mL) was acidified to pH of 2 using

203 0.01 M HCl, then loaded on SPE cartridge, subsequently washed with 1 mL ultrapure

204 water. The HULIS part was retained on the SPE cartridge. 3 mL methanol containing

205 2% ammonia (w/w) was added into SPE cartridge to elute HULIS component, and was

206 evaporated to full dryness with high-pure N_2, followed by dilution with ultrapure water

207 to 25 mL for quantification of HULIS with HPLC coupled with an evaporative light

208 scattering detector (ELSD3000). The recovery efficiency of standard SRFA was 75-

209 80%. More details have been described elsewhere (Tao et al., 2021).

210 2.3.4 Oxidative potential based on DTT assay

211 We detected OP based on previous DTT method (Cho et al., 2005; Lin and Yu,

212 2019) with minor improvements. Briefly, a 1.2 mL portion of sample solution was

213 transferred into 10 mL glass tube, then 6 mL phosphate buffer (0.1 M, pH 7.4) and 300

214 µL of 2.5 mM DTT were added and mixed thoroughly. The samples were placed in a

215 37°C water bath for incubation some time, and reaction was terminated at 30 min

216 intervals over the course of 150 min by taking 1 mL aliquots of DTT mixture and adding

217 100 µL of 5 mM DTNB (prepared in 0.1 mM phosphate buffer) to centrifuge tube. Then,

reaction between DTNB and DTT produced bright yellow TNB, which was quantified using UV-Vis spectrometer within 30 min. Finally, we recorded absorbance (A_t) at 412 nm at time t to quantify indirectly remaining DTT. Another 1.2 mL ultrapure water instead of sample solution was treated in the same way and absorbance was denoted as A for distinguish. A_0 represents initial light absorbance value. Thus, the concentration of DTT consumed by the sample solution (M_{DTT}, μM) and blank solution (M_{DTT0}, μM) were calculated as Eq.(2) and Eq.(3), respectively.

$$M_{DTT} = \frac{A_0 - A_t}{A_0} \times C_{DTT_0} \tag{2}$$

$$M_{DTT0} = \frac{A_0 - A}{A_0} \times C_{DTT_0} \tag{3}$$

Here, C_{DTT0} was initial DTT concentration in sample solution (100 μM in this work). DTT consumption rate (R_{DTT} and R_{DTT0}) was obtained from the slope of plot of M_{DTT} and M_{DTT0} versus incubation time. Experiments of blanks and samples were typically run in a triplicate. The reproducibility of the whole analysis showed that the relative standard deviation of the DTT consumption rate analysis was 3-4%.

2.3.5 Products analysis by GC-MS

Reacted solution (about 30 mL) was extracted with 10 mL dichloromethane twice. The extracts were concentrated to 1 mL using gentle N_2 blow drying, subsequently transferred to a 2 mL vial, and analyzed with a GC-MS (7890A GC/5975C MS, Agilent), using a DB-5ms capillary column (30 m×0.25 mm×0.5 μm). The operational conditions were set as follows: injector at 200°C; ion source at 230 °C; The column oven temperature was programmed: held at 35°C for 4 min, then ramped to 250 °C at a rate of 20°C/min and held for 10 min. The recovery efficiency, method detection limits and quality assurance/quality control has been described in detail elsewhere (Ye et al., 2020).

2.3.6 SP-AMS analysis and aqSOA mass yield

Aerodyne SP-AMS was applied to analyze low volatile organics in reaction solution, similar to our previous work (Chen et al., 2020). AMS data were acquired in V mode and analyzed by Squirrel v.1.56D and Pika v.1.15D software. All the organic fragment ions were classified into six groups: CH, CHO_1, CHN, CHO_2, CHON, HO. Elemental ratios (O/C; hydrogen-to-carbon, H/C), were obtained according to the method proposed by Canagaratna et al. (2015).

Since the AMS analysis requires the nebulization of sample solution into particles before determination, and quantification of organics in each experimental run depend on atomization efficiency and carrier gas flow, we cannot use SP-AMS recorded concentration to quantify aqSOA mass directly. In this case, according to the method suggested by Li et al. (2014), we added an internal standard (SO_4^{2-}) prior to AMS analysis. The ratio of particle-phase organics to SO_4^{2-} ($\Delta Org/SO_4^{2-}$) after atomization represented the relative aqSOA mass. Furthermore, aqSOA mass yield (Y_{SOA}, %), which is generated aqSOA mass per unit mass of precursor consumed, can be calculated as Eq. (4).

$$Y_{SOA}(\%)=\frac{(\Delta Org/SO_4^{2-})[SO_4^{2-}]_0}{C_0 M \eta} \times 100\% \qquad (4)$$

Where $[SO_4^{2-}]_0$ is the initially added SO_4^{2-} concentration (here 7.27 mg·L^{-1}); C_0 is initial eugenol concentration, mmol/L; M is molecular weight of precursor (164 g/mol for eugenol) , η is the degradation rate of eugenol.

3 Results and discussion

3.1 Kinetics of the photo-oxidation

263   Figure 1 shows unreacted eugenol concentrations (c_t) and the negative logarithm

264   of c_t/c_0 (-ln(c_t/c_0)) as a function of reaction time, respectively. Error bars represent one

265   standard deviation from triplicated measurements. As described in Figure 1a, eugenol

266   concentration decreased to be lower than 20% of the initial concentration at 3 h,

267   suggesting photolysis was fast under reaction conditions. In the presence of $^3C^*$,

268   eugenol was degraded to nearly 100% after 3 h. Previous study in our group about $^3C^*$-

269   initiated oxidation of 4-ethylguaiacol (Chen et al., 2020) showed that it degraded

270   completely until 21 h. Apart from difference of target precursor, different light

271   irradiation spectra and stronger energy of light sources in this work might be

272   responsible for the fast decay of eugenol. The BDEs are 340 kJ/mol for OH, 374 kJ/mol

273   for C-H in -CH_3 group, 345 kJ/mol for C-C in C=C bonds, and 403 kJ/mol for C-H in -

274   OCH_3 group, respectively (Herrmann et al., 2003; He et al., 2019). The lowest BDE

275   was found for the O-H bond and C-C bond. Due to the influence of steric hindrance and

276   intramolecular hydrogen bonding, the H-abstraction reaction from the OH group might

277   have been less favorable. The most favorable H-abstraction reaction might have taken

278   place in the C-C in allyl group. As a result of breakage of C=C into C-C at allyl group

279   site, 2-methoxy-4-propyl-phenol could form (See Section 3.6.1). When photon energy

280   is higher than bond dissociation energy, they can directly break chemical bond of

281   molecules, leading to decomposition of compounds and possibly further mineralization.

282   The energies of photons at 313, and 365 nm in our light sources are 395 kJ/mol, and

283   338 kJ/mol, which are higher than the weakest BDEs in eugenol, as a result, eugenol

284   molecule can directly absorb photo energy to decompose.

285   The pseudo-first-order rate constants were obtained by fitting eugenol

286   concentration into the equation under excess oxidants. As shown in Figure 1b, ln(c_t/c_0)

287   is proportional to reaction time, and the first-order rate constants were 2.43×10^{-4} s^{-1},

288   2.73×10^{-4} s^{-1}, and 5.75×10^{-4} s^{-1}, for direct photolysis, •OH-initiated and ^{3}C*-initiated

289   photo-oxidation, respectively. ^{3}C*-initiated photo-degradation was quicker than that

290   with •OH (5.75×10^{-4} s^{-1} vs. 2.73×10^{-4} s^{-1}), which can be attributed to more ROS (such

291   as ^{1}O$_2$, O$_2^-$· and ·OH) participating in ^{3}C*-initiated photolysis. A similar results were

292   found for aqueous phase reaction of three phenols with •OH and ^{3}C* by Yu et al. (2016)

293   who showed degradation rates of three compounds were all higher with ^{3}C* than with

294   •OH.
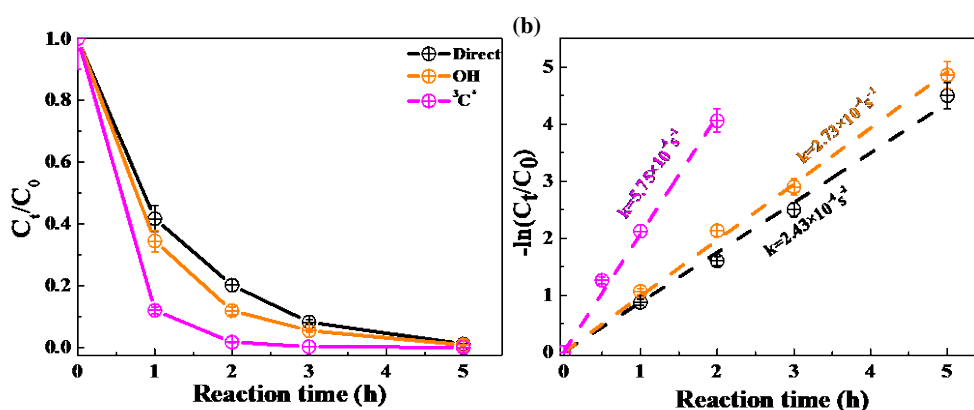
Figure 1. Aqueous-phase eugenol decay kinetic curves (a) and rate constants (b) under three

conditions. Error bars represent one standard deviation from replicated measurements.

3.2 Relative importance of ROS to photo-oxidation

3.2.1 Quenching experiments in ^{3}C*-initiated photo-oxidation

Relative importance of ROS in photo-degradation processes was usually

investigated by the addition of radical quenchers, and here they were calculated based

on the different degradation efficiencies of eugenol in absence and presence of different

ROS quenchers. For each scavenger, we conducted several gradient experiments with

varying molar ratios of eugenol to quenchers. The ratios were set as 0.075:1, 0.15:1,

0.3:1, 0.75:1, 1.5:1 for quenchers of NaN$_3$, TMP and TBA, and 1.2:1, 1.6:1, 2.5:1, 5:1,

306 10:1 for SOD, which were all within the typical range of molar ratios to quench ROS

307 reported previously (Zhou et al., 2018). Above concentrations of the added quencher

308 have been repeatedly adjusted to ensure the complete reactions between radicals and

309 scavengers. Figure 2 displays the effects of different ratios on eugenol degradation. As

310 shown, when adding quenchers into solution, all rate constants (k) were lower than

311 those of the quencher-free solutions. The optimum molar ratios of eugenol to quenchers

312 were selected when the inhibition degree of eugenol degradation unchanged with the

313 increase of added quencher mass (Wang et al., 2021). For example, upon decreasing

314 molar ratios of eugenol to NaN_3 from 1.5:1 to 0.075:1, the inhibitory degree of eugenol

315 degradation was unchanged at ratio of 0.15:1 and 0.075:1, indicating that $^1O_2$ has been

316 absolutely quenched at ratio of 0.15:1, so, we finally selected molar ratios of 0.15:1 for

317 NaN_3, since excess scavenger may produce other products that can change the existing

318 reaction. Finally, the molar ratios of eugenol to quencher TBA, NaN_3, TMP and SOD,

319 of 1.5, 0.15, 0.075 and 2.5, were selected, respectively. Table1 and Figure S1 compared

320 the rate constants determined under various radical quenchers and results showed that

321 rate constants decreased in the order of TMP＞NaN_3＞SOD＞TBA, suggesting relative

322 importance of generated ROS to degradation was in the order of $^3C^*$＞$^1O_2$＞$O_2^{\bullet-}$＞•OH.

323 This result suggests that $^3C^*$ plays a major role in the photo-oxidation reaction. Another

324 study (Laurentiis et al., 2013) on phenol photosensitized by the triplet state of 1-

325 nitronaphthalene (1NN) also showed $^31NN^*$ was capable of degrade phenol via direct

326 reaction with phenol ($^31NN^*$+phOH→$1NN^{-\bullet}$+phO$^\bullet$+H$^+$→products), while both •OH

327 and $^1O_2$ contributions were relatively minor.

328   The value of (k-k$_{TMP}$)/k was 0.857, therefore contribution of $^3C^*$ was estimated to

329 be as high as 85.7%. In the same way, the contributions of $^1O_2$, $O_2^{\bullet-}$ and •OH were

330 80.5%, 61.4% and 53.9%, respectively. The total contribution of the four ROS largely

331 exceeded 100%. This can be explained by the fact that ROS scavengers can actually

332 significantly interrupt the radical chain reactions as compared to those in the absence

333 of scavengers. For instance, the addition of TMP not only scavenge $^3C^*$, but also inhibits

334 $^1O_2$, $O_2^{\bullet-}$, etc. These findings suggest that we cannot directly obtain contributions of

335 each ROS just on basis of the scavenging efficiencies. It should be cautious to apply

336 quenching approach to quantify the role of ROS for pollutant degradation in complex

337 reaction system. Determination of ROS variability during oxidation should be instead

338 by an effective way to elucidate the role of each ROS. Therefore, we tried to detect

339 generated $\bullet OH$, $O_2^{\bullet-}$ and $^1O_2$ during photochemical reaction using a Micro electron spin

340 resonance (ESR) spectrometer (Bruker Magnettech, Berlin, Germany) via DMPO as

341 spin trap to form stable DMPO-$\bullet OH$ or   DMPO-$O_2^{\bullet-}$, TEMP to capture $^1O_2$ to produce

342 TEMP-$^1O_2$ spin-adduct (TEMPO).   The amounts of radicals can be identified and

343 quantified by the peak patterns in EPR spectra, such as quarter line with a height ratio

344 of 1:2:2:1 for DMPO-$\bullet OH$, 1:1:1:1 for DMPO-$O_2^{\bullet-}$ and 1:1:1 for TEMP-$^1O_2$ (Guo et al.,

345 2021). Unfortunately OH radical cannot be detected since the concentrations may not

346 meet the detection limit of the instrument (Fig. S2, ESR spectra of $\bullet OH$). In contrast,

347 we were able to detect higher concentrations of $^3C^*$ and found intensity of TEMP-$^1O_2$

348 signal reached its maximum at 30 min, then decreased slowly (Fig. S2, ESR spectra of

349 $^1O_2$). Combing the greatest inhibitive effect of TMP with high $^1O_2$ concentration from

350 ESR method, we can conclude that $^3C^*$ and $^1O_2$ play relatively important roles in

351 eugenol photo-degradation.

352
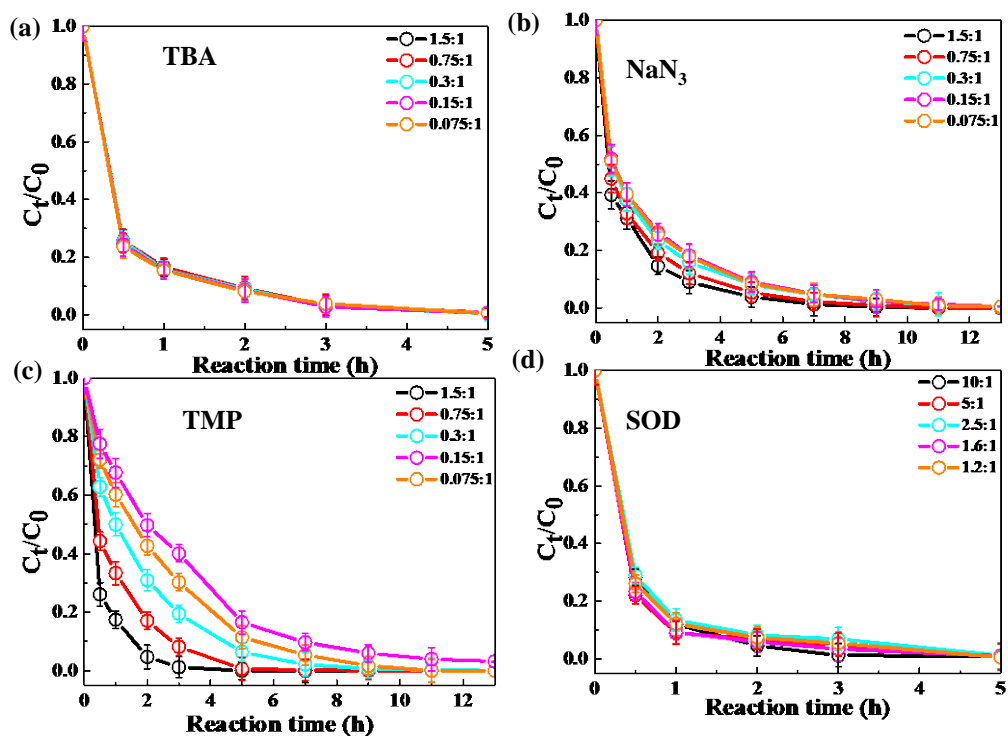
Figure 2. Ratio of residue concentration to initial concentration (C_t/C_0) at different mole ratios as a function of reaction time with (a) TBA quencher, (b) NaN_3 quencher, (c) TMP quencher and (d) SOD quencher. Legend represented mole ratios of eugenol to quenchers.

356

3.2.2 Quenching experiments in OH-initiated photo-oxidation

To examine the contributions of the quenchers to eugenol degradation for OH-initiated oxidation, TBA and *p*-BQ as trapping agent were added. Similar to ${}^3C^*$-initiated oxidation, several gradient experiments via varying molar ratios of eugenol to quenchers were conducted. The ratios were set as 6.5:1, 3.2:1, 1.6:1, 1.1:1 and 0.8:1 for *p*-BQ and 3.0:1, 1.5:1, 0.75:1, 0.3:1 and 0.15:1 for TBA. According to Fig. S3, molar ratio only had a slight influence on eugenol degradation, although degradation can be inhibited effectively by quenchers. So, we finally selected appropriated molar ratios of eugenol to quenchers: 0.8 and 0.75 for *p*-BQ and TBA, respectively, since adding too high concentrations of scavengers can actually influence chemical reaction.

367   Variations in the rate constants for above quenching experiments were calculated,

368 respectively, in comparison with tests conducted without quenchers, and the results

369 were listed in Table 1 and presented in Fig. S4. For TBA quenching tests, the rate

370 constant decreased by 18.7% (from 2.73×10^{-4} s^{-1} to 2.22×10^{-4} s^{-1}), showing that •OH

371 radical played a certain role in eugenol photolysis. Since H_2O_2 was mainly photolyzed

372 at wavelength <300 nm to generate ·OH, but irradiation above 300 nm in this work did

373 not dominate. The p-BQ could quench $O_2^{•-}$, which in turn suppress the generation of

374 other ROS (e.g., $•HO_2$). So, for the p-BQ quenching tests, the rate constant decreased

375 56% (from 2.73×10^{-4} s^{-1} to 1.20×10^{-4} s^{-1}), suggesting $O_2^{•-}$ might be responsible for

376 eugenol degradation. This hypothesis could be further confirmed by the decline of rate

377 constant under N_2-saturated solution shown later. However, it was difficult to detect

378 both •OH and $O_2^{•-}$ directly due to relatively short half-life and low concentration via

379 ESR in this work.

380   **Table 1.** The reaction rate constants of eugenol in the presence of scavengers. The experimentl

381 conditions were as follows: 0.3 mM eugenol, molar ratios of eugenol to quencher TBA, NaN_3, TMP

382 and SOD, of 1.5, 0.15, 0.075 and 2.5 respectively; mole ratio of eugenol to quencher p-BQ and TBA

383 of 0.8 and 0.75 respectively.

$^3C^*$-initiated quenching			
quenchers	ROS	reaction rate constant k (s^{-1})	R^2
no quencher	-	5.75×10^{-4}	0.996
TBA	·OH	2.65×10^{-4}	0.999
SOD	$O_2^{•-}$	2.22×10^{-4}	0.995
NaN_3	$^1O_2$	1.12×10^{-4}	0.999
TMP	$^3C^*$	0.82×10^{-4}	0.999
•OH-initiated quenching			
quenchers	ROS	reaction rate constant k (s^{-1})	R^2
No quencher	-	2.73×10^{-4}	0.995
TBA	·OH	2.22×10^{-4}	0.998
p-BQ	$O_2^{•-}$	1.20×10^{-4}	0.995

384

3.2.3 Influences of different saturated gases

In order to assess the role of O_2, N_2 gas was purged into reaction solution for ~30 min before experiment to achieve deoxygenated condition. Figure 3 compared the eugenol decay variations and rate constants under three saturated conditions for direct photolysis, OH-initiated and $^3C^*$-initiated oxidation, respectively. The insets of the Fig.3a, 3b and 3c show the corresponding rate constants. The rate constants under O_2, air and N_2 followed the order of $k_{O_2} > k_{Air} > k_{N_2}$ under both direct photolysis and •OH oxidation, providing evidence in support of O_2 being responsible for eugenol degradation. This might be explained by the fact that O_2 can act as an electron acceptor to generate $O_2^{•-}$ and •HO_2·, and subsequently form H_2O_2 and •OH. For direct photolysis, rate constant under O_2-saturated condition increased 14.4% while it decreased 19.3% under N_2 saturation, in contrast to the case of saturated air. For OH-initiaed oxidation, the difference of rate constants under three saturated gases became more distinct.

On the contrary, rate constants followed the order of $k_{Air} > k_{N_2} > k_{O_2}$ in $^3C^*$-initiated oxidation system. There are two possible explanations. On the one hand, in N_2-saturated solutions, DMB would be involved in reactions (5-8), followed by more effective generation of $^3DMB^*$. For this reason, eugenol degradation efficiency was higher under N_2 atmosphere than in O_2-saturated solution. On the other hand, in air/O_2 saturated solutions, irradiation of DMB and eugenol would involve reactions (5-12), as a result, $^3DMB^*$ radical decreased, accompanied by the formation of other ROS ($^1O_2$, $O_2^{•-}$, •OH, etc).

$$DMB + h\nu \rightarrow {}^1DMB^* \rightarrow {}^3DMB^* \tag{5}$$

$$^3DMB^* \rightarrow DMB \tag{6}$$

$$^3DMB^* \rightarrow Products \tag{7}$$

$$^3DMB^* + {}^1DMB^* \rightarrow DMB^{\bullet+/\bullet-}(DMB^{\bullet+} + DMB^{\bullet-}) \tag{8}$$

$$^3DMB^* + O_2 \rightarrow DMB + {}^1O_2 \tag{9}$$

$$DMB^{\bullet-} + O_2 \rightarrow \cdot DOM^+ + O_2^{\bullet-} \tag{10}$$

$$O_2^{\bullet-} + 2H^+ \rightarrow H_2O_2 + O_2 \tag{11}$$

$$H_2O_2 \rightarrow 2 \bullet OH \tag{12}$$
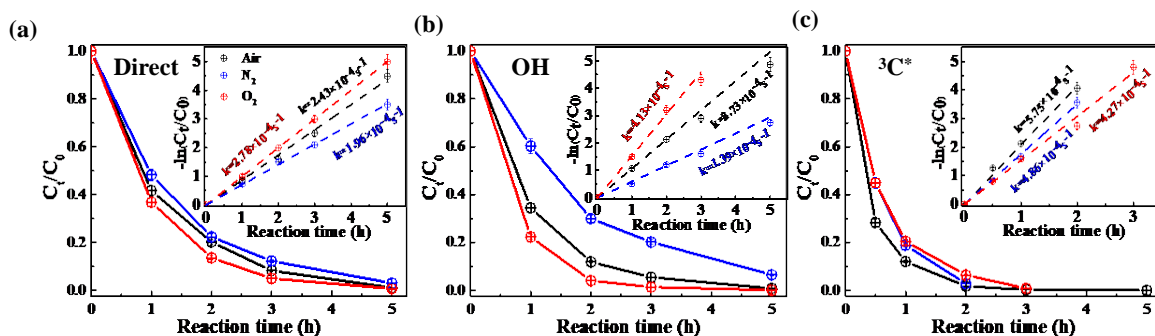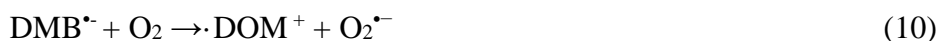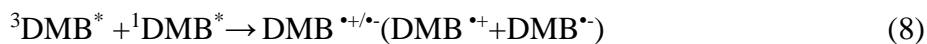
Figure 3. Ratio of remaining concentration to initial concentration (C_t/C_0) as a function of reaction time at different saturated gases under (a) direct photolysis (b) OH-initiated and (c) $^3C^*$-initiated oxidation. Insert plots represented eugenol consumption versus reaction time under different saturated gases: (a) direct photolysis (b) OH-initiated and (c) $^3C^*$-initiated systems.

3.2.4 Variation of pH value and dissolved oxygen (DO)

The initial pH values in directly photolysis and OH-initiated oxidation were unadjusted, while initial pH for the $^3C^*$ system was adjusted to 3. The variation of pH values of reaction solution were presented in Fig.4a. As shown, solution pH values decreased quickly at the initial stage (from 7.40 to ~5.0 at the first 1h) in both direct photolysis and OH-initiated oxidation. However, no obvious decrease of pH value for the $^3C^*$-initiated oxidation could be ascribed to low initial pH value, since in theory slight increase for acidity in solution was hard to influence pH value. Thus, we cannot rule out formation of acid products formation at $^3C^*$-initiated oxidation.

Oxygen can take part in photochemical reaction to form ROS, which may in turn

429   destroy the structure of precursors. In order to further confirm the role of O_2, we

430   measured the oxygen consumption via determining concentration of DO by a dissolved

431   oxygen meter (Seven2Go Pro S9, Zurich, Switzerland) during the photochemical

432   process of eugenol. DO was consumed mainly at the first 1 h and kept stable with the

433   reaction time further increasing (Fig.4b-c and Fig. S5). Percentage of DO concentration

434   consumption followed in the order of $^3C^*$>•OH>direct. The maximum DO consumption

435   for $^3C^*$-initiated oxidation process can be explained by the transfer of electrons from

436     $^3C^*$ to O_2 to form $^1O_2$, which was the major contributor to eugenol degradation. Surely,

437   a steady-state DO level was reached when the consumption rate was equal to the

438   diffusion of O_2 into the solution (Pan et al., 2020).

439   In a word, above experimental results confirmed that O_2 influenced eugenol

440   decomposition and radical conversion via inducing radical chain reactions.

441
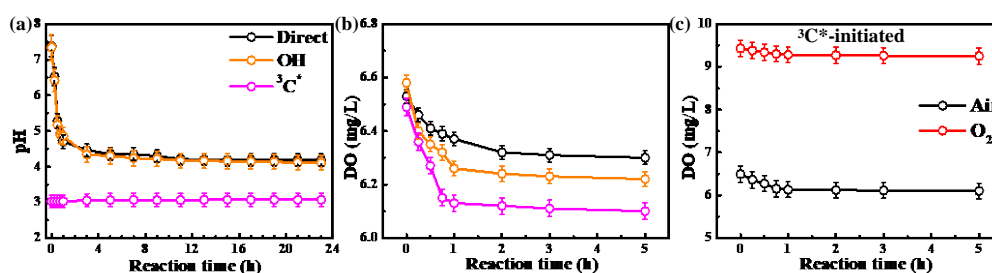
442   **Figure 4.** (a) pH values and (b)-(c) dissolve oxygen as a function of reaction time

443

444 **3.3 Optical properties of photo-oxidation products**

445 **3.3.1 Light-absorbing properties**

446   UV-vis light spectra at different reaction times are presented in Fig. 5. According

447   to UV-Vis spectrum, the maximum photo-absorption wavelength of eugenol was 280

448   nm, indication that wavelength 280 and 350 nm was capable of induce direct

449   photochemical reaction. The wavelength range of photon fluxes in our lamp was over

450   280 and 500 nm, which can meet above condition. Besides, we can clearly observe that

451   the characteristic absorption peak at 280 nm of precursor decreased under all conditions

452   due to the degradation of precursor. As seen in Fig. 5, when adding oxidant H_2O_2, the

453   total variation trend of light absorbance was similar to that without oxidant with some

454   slight difference, for instance at wavelength range of 200-250 nm. However, the

455   reaction was extremely quick in the presence of $^3C^*$, and characteristic absorption peak

456   at 280 nm after 3 h irradiation almost disappeared, suggesting nearly complete depletion

457   of eugenol, which coincided with the results in Section 3.1 that more than 99% eugenol

458   was degraded. However, note that the in $^3C^*$-initiated reaction there was still strong

459   light absorption at wavelength <350 nm, which can be ascribed to the presence of light

460   chromophore DMB or aqSOA products rather than precursor.

461   In particular, there are some differences at wavelength of 300-400 nm in the three

462   systems. For direct photolysis and OH-initiated experiments, light absorbance at 250

463   nm and range of 300-400 nm increased during the first 15 h, then remained at a plateau

464   until 23 h. In contrast, for $^3C^*$-initiated oxidation, light absorbance at above wavelength

465   increased during the first 7 h, then decreased slowly afterwards. The difference plot of

466   UV-Vis spectra between •OH and $^3C^*$-initiated photo-oxidation indicated the formation

467   of different products.

468   The increase of light absorbance at 250 nm upon aqueous photo-processing

469   demonstrates the generation of new substances with both the aromatic C=C and

470   carbonyl (C=O) functional groups, while the enhancement at 300-400 nm suggested the

471   probability of HULIS formation, which could be confirmed later.
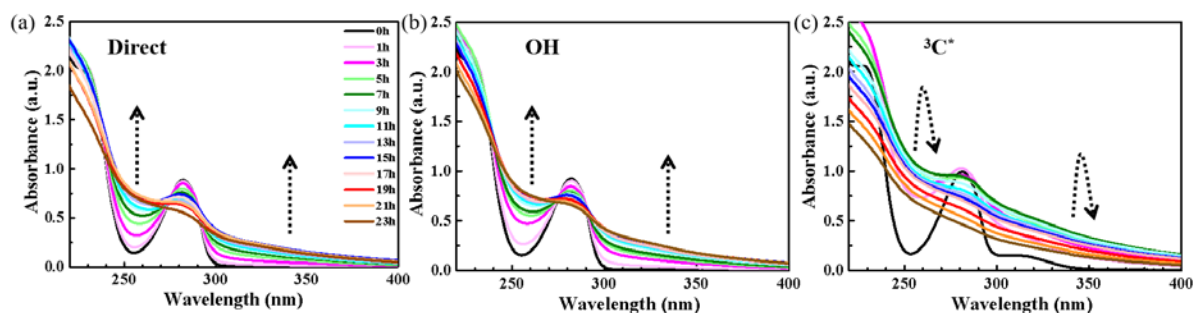
Figure 5. UV–Vis light absorption spectra of reacted solutions at different reaction times under (a)direct photolysis, (b)OH-initiated and (c)^{3}C*-initiated systems.

3.3.2 Fluorescence properties

The variation of fluorescence intensities of solutions before (0 h) and upon photolysis (3 h and 7 h) were investigated via the EEM technique, as shown in Fig.6. For comparison, we also presented EEM profiles of pure eugenol (non-irradiated solution), pure DMB, and the end solutions (23 h) of direct photolysis and OH-initiated oxidation in Fig. S6. The peaks at Ex/Em=275/313 nm are ascribed to fluorescence of phenolic structure of parent substance, as suggested by Laurentiis et al. (2013). As shown in both Figure 6 and Figure S6, the fluorescence intensity from parent substance decreased after photolysis due to eugenol decay, and the decreasing trend was very fast for ^{3}C*-initiated oxidation. This results matched with the fast photolysis and large rate constant for ^{3}C*-initiated oxidation. The EEM plots for direct photolysis and OH-initiated reaction had similar contour patterns as shown in Fig.6 a and b across the entire photochemical reaction, although EEM profile changed significantly with irradiation time. We also observed distinct fluorescent peaks at Ex/Em=235 /400-500 nm, indicating that irradiation caused a red shift in fluorescence emission wavelength. As suggested by Chang et al. (2010), fluorophores at Ex/Em=240/400 nm was linked to aromatic structures and condensed saturated bonds including polycyclic aromatic

hydrocarbons. Another work (Li et al., 2021) showed that red shift in the fluorescence spectra was usually related to an increase in the size of the ring system and an increase in the degree of conjugation. Previous studies (Chen et al., 2016a; Chen et al., 2019; Wu et al., 2019) have reported that fluorescent compounds with emission wavelength at 400-500 nm may be highly oxygenated species such as HULIS. Additionally, HULIS have two typical florescent peaks in EEM plots at Ex/Em=200-300/400-500nm and Ex=Em=350/400-500nm with more intense for Ex of 200-300nm (Laurentiis et al., 2013; Vione et al., 2019; Wu et al., 2021). So, we inferred that new peak at Ex/Em=235 /400-500 nm likely attributed to chromophores of HUILS. However, for the $^3C^*$- initiated reaction, extra fluorescent peaks at Ex/Em=220-300 nm/400-500nm also appeared at the first 1 h (data not shown), but their intensities were much weaker and gradually disappeared upon prolonged photolysis (3 h). Previous study (Laurentiis et al., 2013) from photosensitise of phenol (nitronaphthalene as photosensitizer) also showed significant increase of HULIS fluorescence signal at Ex/Em=330/415nm. Anyway, EEM results were difficult to interpret because of many complicated substances in reaction samples that might contribute to absorption and emission at certain excitation wavelength, and it is hard to distinguish and isolate fluorescent and nonfluorescent constituents via current techniques.

Another interesting finding was that a small fluorescence peak appeared at Ex/Em=300-350/300-350 nm at different reaction stages. Specifically, it appeared earlier for $^3C^*$ oxidation (at 3 h) than other two systems, and the peak seemed to be a bit stronger in the end solutions of direct photolysis and OH oxidation (Fig. S6). One unexpected phenomenon in the EEM spectra here is the absence of fluorescence at higher excitation wavelengths (>350 nm), which is often observed in aerosol particles (Wu et al., 2021). This could be attributed to different precursor and aqueous reaction

517 mechanisms (Xie et al. 2016).

518   Note that uncertainties still exist in using EEM fluorescence technique to

519 characterize aqSOA due to lack of standard EEM profile for specific products of

520 aqueous phase oxidation and clearly more studies are needed in future.

521
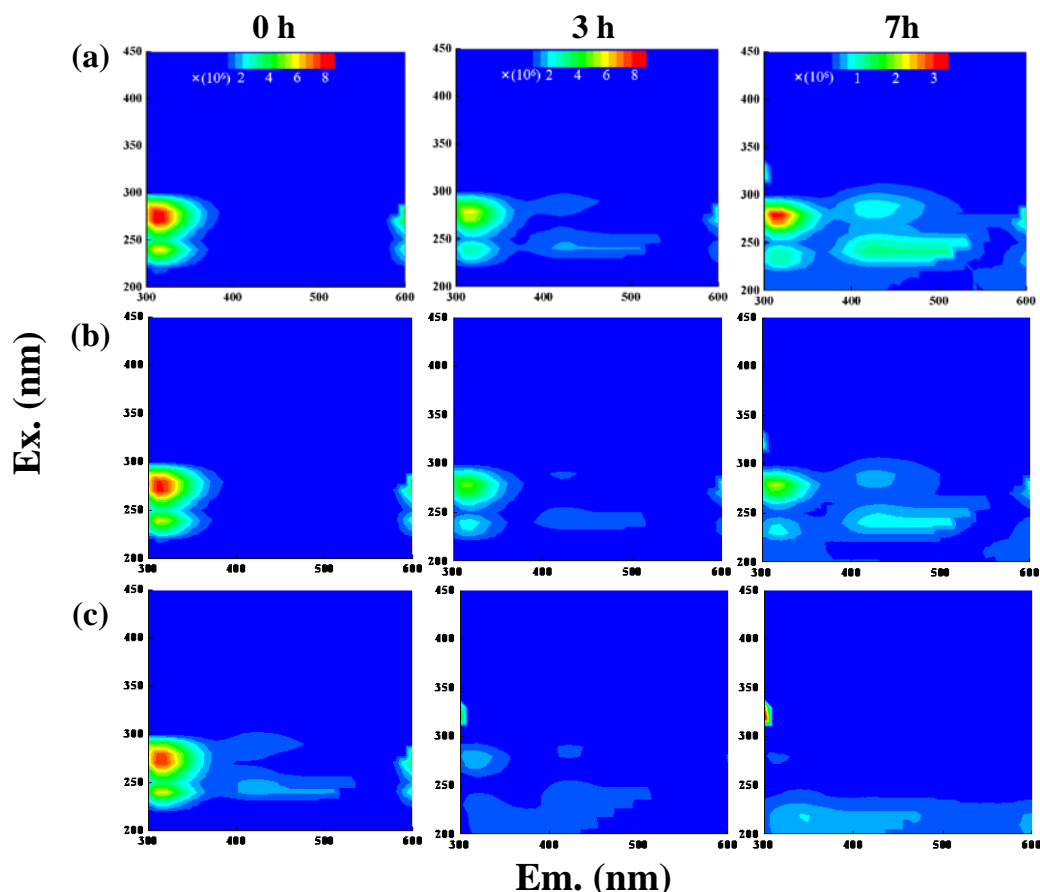
522 **Figure 6.** EEM fluorescence spectra of the initial solution (0 h) and those at different reaction time

523 (3 h and 7 h) under (a) direct photolysis, (b) OH-initiated and (c) $^3C^*$-initiated oxidation. The top

524 color bar represents the range of fluorescence intensity.

525 **3.4 HULIS concentration determination**

526   The EEM spectra found new prominent fluorescent peak at Ex/Em=250 nm/400-

527 500 nm, which was likely attributed to chromophores of HUILS according to results

528 from Section 3.3.2. However, EEM technique cannot directly distinguish products

529 solely based on the shapes and limited information of the EEM profiles. Here we

530 determined the HULIS concentrations in the oxidized solutions by using the HPLC

531 method. Figure 7 presented the measured HULIS concentrations as a function of

532 reaction time for all three systems. The results show clearly that aqueous-phase eugenol

533 oxidation can produce HULIS, and the amount increased gradually in the first 7 h, then

534 remained at a similar level (about 30 mg/L) later in the OH-initiated system. For direct

535 photolysis, HULIS concentration increased until 11h and then retained steady at a level

536 around 40 mg/L. For the $^3C^*$ oxidation, HULIS concentration increased to its maximum

537 at 7 h, but it decreased slightly afterwards. The possible reason was that generated

538 HULIS was capable of further taking part in photochemical reactions. Study from Smith

539 (2015) suggest different reaction mechanisms between aqueous benzene-diols with $^3C^*$

540 and OH radical, with $^3C^*$ oxidation producing higher molecular weight products with

541 less fragmentation. Thus, we inferred that more higher molecular weight HULIS

542 products were formed at the first stage.

543
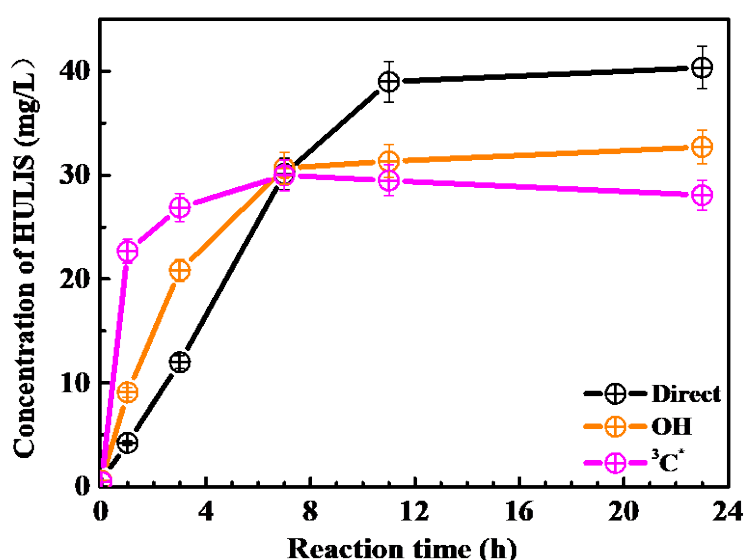
544 **Figure 7.** HULIS concentrations as a function of reaction time for the three systems

545 **3.5 aqSOA mass yield and oxidation degree**

3.5.1 aqSOA mass yield

Figure 8a showed SP-AMS measured organic mass profiles (normalized by sulfate mass, $\Delta Org/SO_4^{2-}$) against the reaction time. As the reaction propagates, $\Delta Org/SO_4^{2-}$ increased continuously in $^3C^*$-initiated system. Nevertheless it rose gradually and reached a maximum at 19 h, then remained at a plateau for the direct photolysis and OH-initiated oxidation. Figure 8b illustrated the aqSOA mass yields at different reaction times for the three systems. The aqSOA mass yields after 1h illumination were in the ranges of 46.2%-196.5%, 22.1%-144.9%, 19.3%-140.1% for $^3C^*$, OH and direct photolysis, respectively. And, for the same oxidation time, mass yields from $^3C^*$-oxidation were generally higher than those from OH-initiated oxidation, which were on the other hand, higher than those from direct photolysis.

The aqSOA mass yields in OH-initiated oxidation of this work agree well with that reported previously for phenolic carbonyls, that is, 120% for syringaldehyde (Huang et al., 2018). Our previous study on eugenol OH oxidation illuminated by a 500 W Xe lamp reported the aqSOA mass yield of ~180% for eugenol (Ye et al., 2020), slightly higher than the value reported in this work.
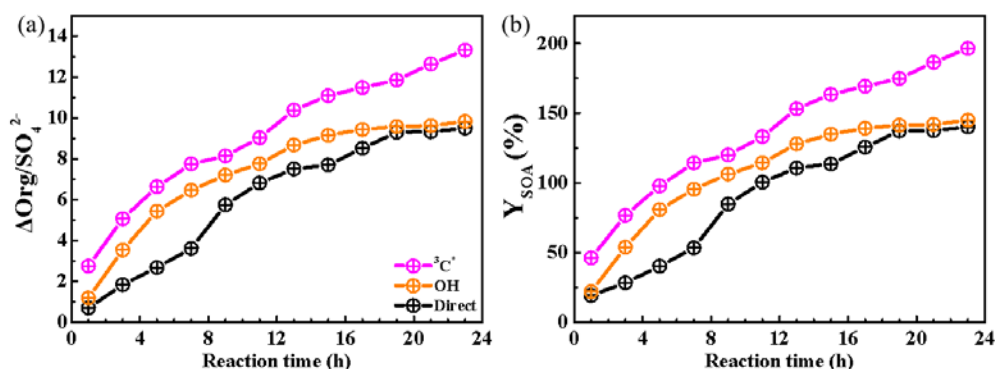
Figure 8. Variations of the aqSOA mass normalized by sulfate (a) ($\Delta Org/SO_4^{2-}$) and (b) aqSOA mass yields under three photo-oxidation conditions.

3.5.2 Oxidation degrees of aqSOA

In order to further represent the oxidation levels of the aqSOA, O/C derived from SP-AMS measured mass spectrum of the organics was used to assess oxidation degree of aqSOA. In addition, carbon oxidation state (OSc, defined as 2*O/C - H/C) was also calculated (Kroll et al., 2011). Figure 9a-c described the temporal variations of the elemental ratios (O/C and H/C) and OSc during oxidation in the three systems.

Dramatic increases of O/C and OSc in the initial stage of oxidation (within 1 hour) were observed, with O/C changed from 0.26 to 0.65, from 0.26 to 0.70, from 0.25 to 0.75, as well as OSc changed from -1.11 to -0.15, from -1.16 to -0.05, from -1.13 to 0.09 for direct photolysis, OH-initiated and ^{3}C*-initiated oxidation, respectively. Correspondingly, there was a clear drop of H/C in the first hour of oxidation for all three systems as well. Afterwards, both O/C and OSc gradually increased while H/C did not change significantly. Similarly, aqSOA from ^{3}C*-oxidation had higher levels of oxidation degrees (both O/C and OSc) than that from OH-oxidation, whose values were higher than that from direct photolysis. The enhancements of OSc in the final solutions were 1.22, 1.11 and 0.86 for ^{3}C*-initiated oxidation, OH-initiated oxidation and direct photolysis, respectively.

Furthermore, the f_{44} vs. f_{43} diagrams (termed as "triangle plot") can be used to demonstrate the evolution of aqSOA during oxidation (Fig. 9d-f). The f_{44} and f_{43} are defined as the ratios of signal intensities of m/z 44 and 43 to the total organics. The results showed that the f_{44} rose continuously (moved upwards) during ·OH and ^{3}C* oxidations, indicating persistent formation of organic acids, such as formic acid and oxalic acid (Sun et al., 2010). Note the f_{44} enhancement was again much more significant for ^{3}C* oxidation (from 0.07 to 0.16) than direct photolysis (from 0.08 to 0.12) and ·OH oxidation (from 0.07 to 0.13), consistent with the behaviors of O/C and

590 OSc. However, f_{43} values actually decreased in the first 3h for direct photolysis and

591 OH-initiated oxidation, and then increased at the later stages; while for the $^3C^*$-initiated

592 oxidation, it only decreased in the first hour. Note that all data points located outside

593 the f_{44} vs. f_{43} space observed for ambient aerosol AMS dataset established by Ng et al.

594 (2010), owing to the relatively lower f_{43} values.

595 In summary, our results shown here demonstrate that aqueous phase eugenol

596 photochemical oxidation can generate highly oxygenated products and hence increase

597 the degree of oxygenation of overall SOA.

598
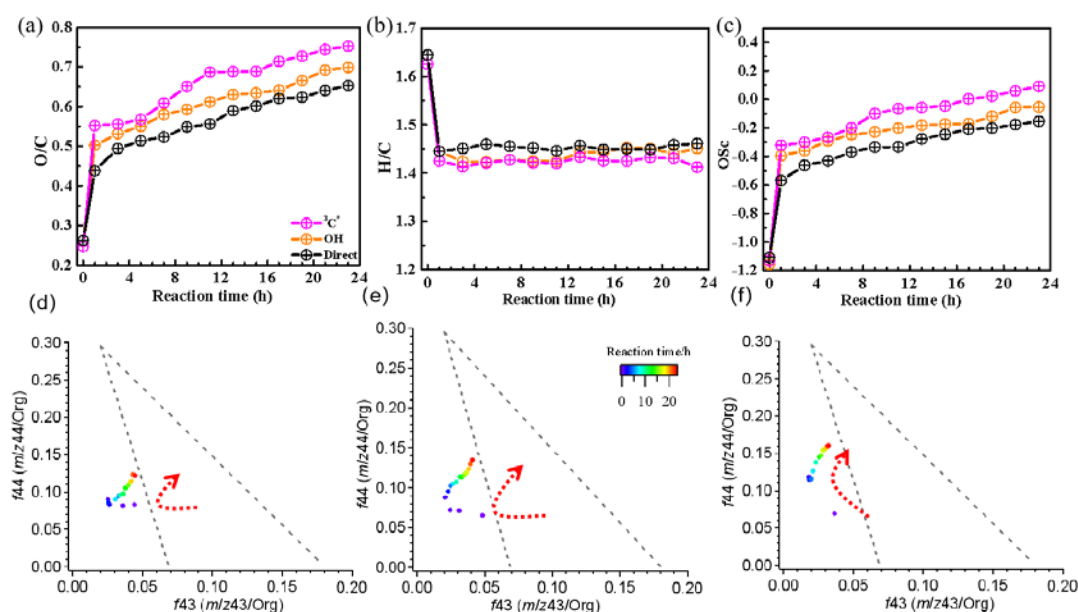
599 **Figure 9.** Variations of elemental ratios (a-c) (H/C, O/C) and OSc as a function of reaction time,

600 and the "Triangle plot" of aqSOA (d-f) under direct photolysis, OH-initiated and $^3C^*$-initiated

601 oxidations.

602 **3.6 Molecular characterization of products and proposed reaction mechanism**

603 **3.6.1 Molecular characterization by GC-MS**
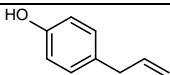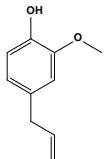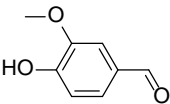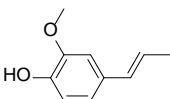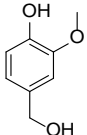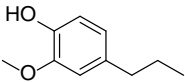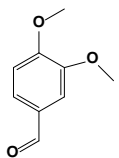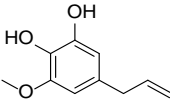
604 SP-AMS was limited to probe bulk composition of low-volatility oxidation

605 products, and the molecular characterization of products was performed by using GC-
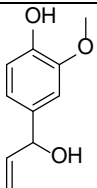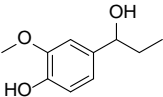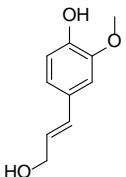
MS here. For example, the total ion chromatograph (TIC) of GC-MS on the solutions before oxidation (0 h) and at illumination times of 11 and 23 h for the $^3C^*$-initiated system is shown in Fig. S7. Eugenol (retention time (RT) at 11.50 min) loss was more than 90% at 11 h, which could be confirmed by the experimental data reported in Section 3.1. Comparison of products at 11 h and 23 h showed no significant difference. Similar to results reported by our previous work (Ye et al., 2020) on the eugenol but with OH as oxidant, a series of products, including 2-methoxy-4-methylphenol (molecular weight (MW) 138, RT=10.27 min), vanillin (MW 152, RT=11.79 min), (E)-2-methoxy-4-propenyl-phenol (MW 164, RT=12.06 min), 4-hydroxy-3-methoxybenzyl alcohol (MW 154, RT=12.11 min), 2-methoxy-4-propyl-phenol (MW 166, RT=12.18 min), 1-(4-hydroxy-3-methoxyphenyl)-2-propanone (MW 180, RT=12.65 min), 4-(1-hydroxypropyl)-2-methoxyphenol (MW 182, RT=12.73 min), (E)-4-(3-hydroxyprop-1-en-1-yl)-2-methoxyphenol(MW 180, RT=12.91 min) and 4-allyl-methoxybenzene-1,3-diol (MW 180, RT=13.20 min) were identified in the OH-initiated system. However, two additional compounds, 4-hydroxy-3-methoxy-mandelic acid (MW 198, RT=12.79 min) and 3,4-dihydroxy-, methyl ester-benzoicacid (MW 168, RT=13.39 min) were also detected. The product 1-(4-hydroxy-3-methoxyphenyl) with a carbonyl group was relatively abundant. Overall, there are little differences between products identified in this work and those in our previous work (Ye et al., 2020), despite the different light sources and oxidants.

The molecular formulas, molecular weights, proposed structures, and identities of the major products (9 compounds) are listed in Table 2 for the $^3C^*$-initiated system.. Except 5-ally-3-methoxybenzene-1,2-diol(MW 180, RT=12.59 min), the other eight products were also detected in the OH-initiated system. Products were mainly from addition/elimination of hydroxyl (-OH), methoxyl (-OCH$_3$) to benzene ring or allyl

631 group and further oxidation to carbonyl compounds, such as 4-hydroxy-3-

632 methoxybenzaldehyde.

633 **Table 2.** Products identified via GC-MS detection under $^3C^*$ system

	RT (min)	Material name	Chemical structure	Chemical formula	MW (g/mol)
Product 1	10.68	4-allylphenol		$C_9H_{10}O$	134
Precursor (Eugenol)	11.50	Eugenol		$C_{10}H_{12}O_2$	164
Product 2	11.81	4-hydroxy-3-methoxybenzaldehyde		$C_8H_8O_3$	152
Product 3	12.06	(E)-2-methoxy-4-(prop-1-en-1-yl)phenol		$C_{10}H_{12}O_2$	164
Product 4	12.11	4-(hydroxymethyl)-2-methoxyphenol		$C_8H_{10}O_3$	154
Product 5	12.18	2-methoxy-4-propylphenol		$C_{10}H_{14}O_2$	166
$^3C^*$ precursor (DMB)	12.29	3,4-dimethoxybenzaldehyde		$C_9H_{10}O_3$	166
Product 6	12.59	5-allyl-3-methoxybenzene-1,2-diol		$C_{10}H_{12}O_3$	180

Product 7	12.65	4-(1-hydroxyallyl)-2-methoxyphenol		$C_{10}H_{12}O_3$	180
Product 8	12.79	4-(1-hydroxypropyl)-2-methoxyphenol		$C_{10}H_{14}O_3$	182
Product 9	12.91	(E)-4-(3-hydroxyprop-1-en-1-yl)-2-methoxyphenol		$C_{10}H_{12}O_3$	180

3.6.2 Reaction mechanism

634

635 Based on the GC-MS results, the reaction pathways of $^3C^*$-initiated photo-

636 oxidation of eugenol are demonstrated in Scheme 1. To better describe pathways, DMB

637 were expressed as [RCHO] and eugenol as Ph-R for simplicity. First, [RCHO] absorbs

638 light and undergo excitation to $^1[RCHO]^*$, then experiences the intersystem crossing

639 (ISC) to $^3[RCHO]^*$. The $^3[RCHO]^*$ can participate in later reactions via three channels.

640 First, it can react with O_2 to form $^1O_2$ via energy transfer. Secondly, it can become to

641 $[RCHO]^{\bullet-}$, subsequently react with O_2 to generate $O_2^{\bullet-}$ via electron transfer, which can

642 disproportionate to H_2O_2. The decomposition of H_2O_2 can generate OH radical. Thirdly,

643 the $^3[RCHO]^*$ can react with Ph-R to from [Ph-R•] via H-abstraction.

644 As the activated intermediate [Ph-R•] was formed, it could transfer to a myriad of

645 products by several reaction pathways. One important route is the cleavage of [Ph-R•],

646 by dissociating into a free radical segment, such as $CH_2CH\bullet$ or $CH_3O\bullet$. Once the $CH_3O\bullet$.

647 is formed, an addition hydrogen transfer would happen, resulting in a 2H-addition to

648 the new intermediate to form 4-allyl-phenol (product 1). Similarly, when the $CH_2CH\bullet$

649 is lost, an addition of H_2O would happen on the new compound (Product 4) and further

oxidized to 4-hydroxy-3-methoxybenzaldehyde (product 2). Another possibility is the intermediate [Ph-R•] could resonate to several different isoelectronic species, the radical position changing to aromatic ring or allyl group site, which would couple with HO• to form hydroxylated eugenol monomer (product 6, 7, 9 MW=180). Furthermore, the isoelectronic species at allyl group site could also abstract a hydrogen to form isoeugenol (product 3 MW=164). Also, breakage of C=C into C-C and 2H-addition at allyl group site could form 2-methoxy-4-propyl-phenol (product 5, MW=166). Besides, the C=C breaking intermediate can couple with HO• to form 4-(1-hydroxypropyl)-2-methoxyphenol (product 8, MW=182). In conclusion, $^3C^*$ can oxidize eugenol via energy transfer, electron transfer, hydrogen abstraction, proton-coupled electron transfer or other radical chain reactions. Among them, electron transfer appear to be the dominant reaction mechanism.

The organic groups, such as methoxy, allyl groups can be eliminated from aromatic ring, which then participate in photochemical reaction, resulting in generation of dimers, small organic acids, CO_2 and H_2O, et al. No dimers were detected in the products via GC-MS but by SP-AMS with trace amounts. The reason might be because the allyl group is very active due to presence of C=C double bond, providing more attacking points, favoring more functionalization and fragmentation reactions.

668
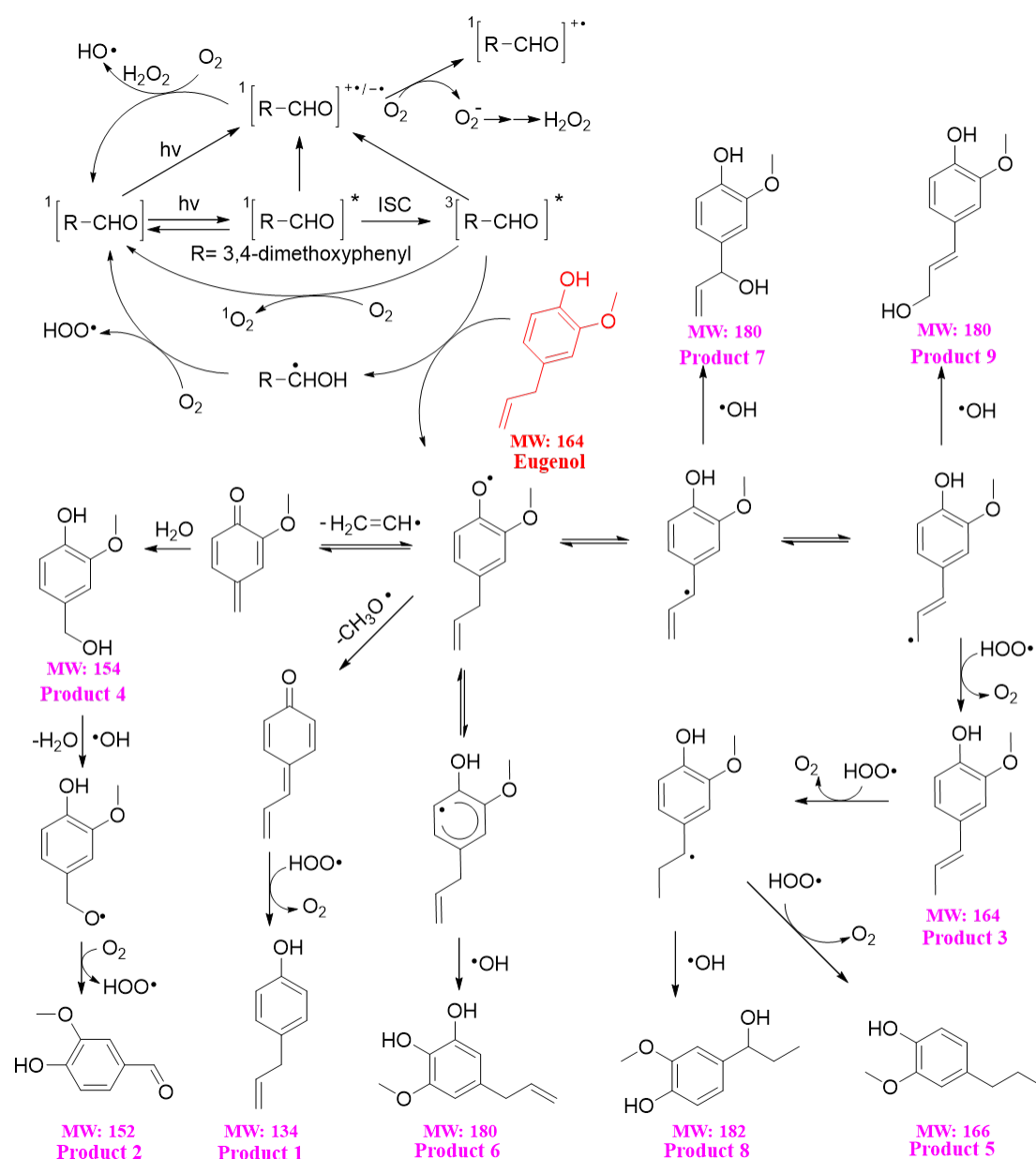
669   **Scheme 1.** Proposed eugenol $^3C^*$-initiated reaction mechanism. The red text represents the

670   compounds listed in Table 1 identified by the GC-MS.

3.7 Oxidative potential of products

672   Previous studies (Chen et al., 2021; Verma et al., 2015b) have confirmed that

673   HULIS are a major contributor to DTT activity, and HULIS were formed upon aqueous

674   photolysis of eugenol in this work. Based on above results, we want to know whether

675   or not there are some links between DTT activity and HULIS concentration. So, we

detected the OP variation with reaction time. The OP of aqueous phase products can be represented by the consumption rate of DTT concentration per minute, defined as R_{DTT}. Figure 10a shows the DTT consumed mass (M_{DTT}) as a function of incubation times (0, 30, 60, 90, 120 and 150 mins) for a triplicate sample (300 μM eugenol) and blank (ultrapure water). As shown in Figure 10a, M_{DTT} for both blank and eugenol sample were proportional to incubation time, indicating that ROS-generating substance in reaction solution acts only as catalyst and was itself not consumed. The slopes represented DTT consumption rates, which were also illustrated in Fig. 10a. According to Fig. 10a, we obtained average R_{DTT0} (blank) of 0.31 μM/min and R_{DTT} for initial 300 μM eugenol (before experiment) of 0.52 μM/min. According to other work, the self-oxidation of DTT might lead to the consumption of DTT in ultrapure water. Final DTT consumption rate for reaction solution after photolysis was then blank-corrected by subtracting average R_{DTT0}.

Figure 10b shows changes of blank-corrected R_{DTT} with photolysis time for direct photolysis, OH-initiated oxidation and $^3C^*$-initiated oxidation, respectively. The R_{DTT} value of $^3C^*$-oxidation system increased quickly and reached the maximum (0.9) at 7 h, then decreased slowly but its end value was slower than that from OH-oxidation. The R_{DTT} value of OH-oxidation system on the other hand increased slowly and reached the maximum at 21 h. The R_{DTT} value of direct photolysis system increased continuously but also slowly to ~0.36 till the termination of oxidation. Nevertheless, In all systems, we can see that the R_{DTT} value after oxidation was higher than that of initial eugenol, providing evidence that aqueous oxidation products increases oxidative potential, resulting in more significant health effects than the precursor compounds especially for $^3C^*$-initiated photolysis. The DTT consumption rates are comparable to those reported by other researchers using the same DTT method (Charrier and Anastasio, 2012; Lin

and Yu, 2019). This finding further indicates the effectiveness of DTT method to represent OP of aqueous-phase photolysis.
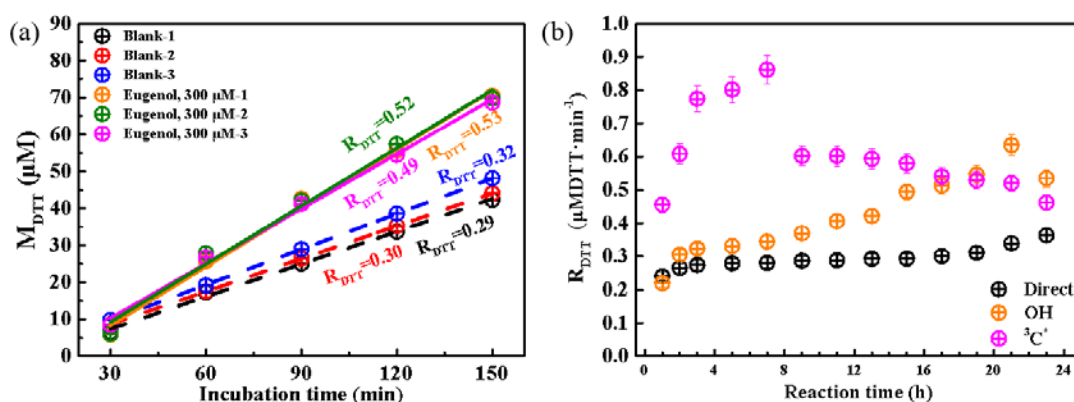
Figure 10. (a) DTT consumption mass versus incubation time for blanks and 300 μM eugenol in triplicate experiments (b) blank-corrected DTT consumption rate versus reaction time for direct photolysis, OH and $^3C^*$ induced oxidation.

4. Conclusions

This work systematically investigated the aqueous photo-oxidation of eugenol. We conducted a comprehensive analysis of the degradation kinetics of eugenol, chemical and optical analysis as well as toxicity (oxidative potential) of the products under direct photolysis, $OH/^3C^*$-initiated oxidation processes. Our results showed eugenol decay the fastest in $^3C^*$-initiated photo-oxidation. With the combination of quenching experiments, ESR method and different saturated gas experiments, it can be concluded that both $^3C^*$ and $^1O_2$ were responsible for eugenol degradation in $^3C^*$-initiated oxidation, while both O_2 and $O_2^{\bullet-}$ played crucial role in OH-initiated reaction. Interestingly, O_2 can inhibit eugenol degradation by effectively quenching $^3C^*$ radical while it can promote degradation by foster radical chain reactions. Above experimental results also offered us an insight into the degradation mechanism of eugenol involved with ROS. It can also serve as the basis for controlling reaction pathway through

720 regulating the ROS generation during aqueous reaction.

721   Light absorbance at wavelength of 300-400 nm in UV-vis spectra increased with

722 photolysis time. EEM spectra displayed fluorescent peak shifted to the long wavelength

723 range as reaction progresses. Distinct peak at Ex/Em=250/400-500 nm displayed upon

724 irradiation under direct photolysis and OH-initiated experiments. Those results all point

725 out the generation of brown carbon and fluorophores, such as HULIS. HULIS

726 determination confirmed that HULIS was formed continuously over photolysis. In

727 addition, DTT consumption rate of products was in the order of $^3C^*$>OH>direct,

728 suggesting that oxidative stress of products was higher in $^3C^*$-initiated photolysis

729 process. The present work for the first time investigated the fluorescent properties and

730 oxidative potential of aqueous phase photo-oxidation products of eugenol, and results

731 showed that EEM fluorescence would be an extremely useful tool to assess the

732 formation of humic-like substances.

733   SP-AMS data showed that oxidation degree of aqSOA increased as photolysis

734 propagated, suggesting formation of highly oxidized products as well as low-volatility

735 products. A variety of products were detected via GC-MS. We then proposed that

736 functionalization was the predominant pathway throughout entire aqueous eugenol

737 oxidation.

738   In future, the relationship between EEM components and chemical structure of

739 HULIS must be studied statistically via advanced analysis method. Furthermore, to

740 elucidate the role of each ROS, we should investigate the time-dependent variation of

741 all ROS via high-sensitivity EPR.

742

743 **Data availability.** The data in this study are available from the authors upon request

744 (bess_ye@jsut.edu.cn or caxinra@163.covm)

745   *Supplement.* **The supplement related to this article is available on line at:**

746

747   *Author Contributions:* XDL, YT, LWZ, SSM, SPL, ZZZ and NS conducted the

748   experiments. XDL and YT analyzed the data. XDL and ZLY prepared and wrote the

749   paper with contributions from all co-authors. ZLY and XLG reviewed and commented

750   on the paper.

751   *Competing interests.* The authors declare that they have no conflict of interest.

752

753   *Acknowledgements.* This authors acknowledge support from the National Natural

754   Science Foundation of China (21976093 and 42021004), the Natural Science

755   Foundation of Jiangsu Province (BK20181476), open fund by Jiangsu Key Laboratory

756   of Atmospheric Environment Monitoring and Pollution Control (KHK1904) and the

757   Postgraduate Research & Practice Innovation Program Jiangsu Province

758   (SJCX21_1332, SJCX20_1030) and of Jiangsu University of Technology

759   (XSJCX20_05).

760   *Financial support:* This research was funded by the National Natural Science

761   Foundation of China (21976093 and 42021004), the Natural Science Foundation of

762   Jiangsu Province (BK20181476), and open fund by Jiangsu Key Laboratory of

763   Atmospheric Environment Monitoring and Pollution Control (KHK1904).

764

References

766   Alam, M. S., Delgado-Saborit, J. M., Stark, C., and Harrison, R. M.: Using atmospheric measurements

767   of PAH and quinone compounds at roadside and urban background sites to assess sources and

768   reactivity, Atmos. Environ., 77(3), 24-35, https://doi.org/10.1016/j.atmosenv.2013.04.068, 2013.

769   Alegría, A. E., Ferrer, A., Santiago, G., Sepúlveda, E., and Flores, W.: Photochemistry of water-soluble

770 quinones. Production of the hydroxyl radical, singlet oxygen and the superoxide ion, J.

771 Photochem. Photobiol. Chem., 127, 57-65, https://doi.org/10.1016/S1010-6030(99)00138-0,

772 1999.

773 Arakaki, T., Anastasio, C., Kuroki, Y., Nakajima, H., Okada, K., Kotani, Y., Handa, D., Azechi, S.,

774 Kimura, T., Tsuhako, A., and Miyagi, Y.: A general scavenging rate constant for reaction of

775 hydroxyl radical with organic carbon in atmospheric waters, Environ. Sci. Technol., 47, 8196-

776 8203, https://doi.org/10.1021/es401927b, 2013.

777 Aryal, R., Lee, B. K., Beecham, S., Kandasamy, J., Aryal, N., and Parajuli, K.: Characterisation of road

778 dust organic matter as a function of particle size: A PARAFAC Approach, Water Air Soil Poll. ;

779 226, https://doi.org/10.1007/s11270-014-2289-y, 2015.

780 Canagaratna, M. R., Jimenez, J. L., Kroll, J. H., Chen, Q., Kessler, S. H., Massoli, P., Hildebrandt Ruiz,

781 L., Fortner, E., Williams, L. R., Wilson, K. R., Surratt, J. D., Donahue, N. M., Jayne, J. T., and

782 Worsnop, D. R.: Elemental ratio measurements of organic compounds using aerosol mass

783 spectrometry: characterization, improved calibration, and implications, Atmos. Chem. Phys.,

784 15, 253-272, https://doi.org/10.5194/acp-15-253-2015, 2015.

785 Chang, J. L., and Thompson, J. E.: Characterization of colored products formed during irradiation of

786 aqueous solutions containing H_2O_2 and phenolic compounds, Atmos. Environ., 44, 541-551,

787 https://doi.org/10.1016/j.atmosenv.2009.10.042, 2010.

788 Charrier, J. G., and Anastasio, C.: On dithiothreitol (DTT) as a measure of oxidative potential for ambient

789 particles: evidence for the importance of soluble transition metals, Atmos. Chem. Phys. 12,

790 9321-9333, https://doi.org/10.5194/acp-12-9321-2012, 2012.

791 Chen, Q., Ikemori, F., and Mochida, M.: Light Absorption and excitation-emission fluorescence of urban

792 organic aerosol components and their relationship to chemical structure, Environ. Sci. Technol.,

793 50, 10859-10868, https://doi.org/10.1021/acs.est.6b02541, 2016a.

794 Chen, Q., Miyazaki, Y., Kawamura, K., Matsumoto, K., Coburn, S., Volkamer, R., Iwamoto, Y., Kagami,

795 S., Deng, Y., Ogawa, S., Ramasamy, S., Kato, S., Ida, A., Kajii, Y., and Mochida, M.:

796 Characterization of chromophoric water-soluble organic matter in urban, forest, and marine

797 aerosols by HR-ToF-AMS analysis and excitation-emission matrix spectroscopy, Environ. Sci.

798 Technol., 50, 10351-10360, https://doi.org/10.1021/acs.est.6b01643, 2016b.

799 Chen, Q., Wang, M., Wang, Y., Zhang, L., Li, Y., and Han, Y.: Oxidative potential of water-soluble matter

associated with chromophoric substances in $PM_{2.5}$ over Xi'an, China, Environ. Sci. Technol., 53, 8574-8584, https://doi.org/10.1021/acs.est.9b01976, 2019.

Chen, Y., Li, N., Li, X., Tao, Y., Luo, S., Zhao, Z., Ma, S., Huang, H., Chen, Y., Ye, Z., and Ge, X.: Secondary organic aerosol formation from $^3C^*$-initiated oxidation of 4-ethylguaiacol in atmospheric aqueous-phase, Sci. Total. Environ., 723, 137953, https://doi.org/10.1016/j.scitotenv.2020.137953, 2020.

Cho, A. K., Sioutas, C., Miguel, A. H., Kumagai, Y., Schmitz, D. A., Singh, M., Eiguren-Fernandez, A., and Froines, J. R.: Redox activity of airborne particulate matter at different sites in the Los Angeles Basin, Environ. Res., 99, 40-7, https://doi.org/10.1016/j.envres.2005.01.003, 2005.

De Laurentiis, E., Sur, B., Pazzi, M., Maurino, V., Minero, C., Mailhot, G., Brigante, M., and Vione, D.: Phenol transformation and dimerisation, photosensitised by the triplet state of 1-nitronaphthalene: A possible pathway to humic-like substances (HULIS) in atmospheric waters, Atmos. Environ., 70, 318-327, https://doi.org/10.1016/j.atmosenv.2013.01.014, 2013.

Dou, J., Lin, P., Kuang, B. Y., and Yu, J.: Reactive oxygen species production mediated by humic-like substances in atmospheric aerosols: enhancement effects by pyridine, imidazole, and their derivatives, Environ. Sci. Technol., 49(11), 6457-6465, https://doi.org/10.1021/es5059378, 2015.

Ervens, B., Turpin, B. J., and Weber, R. J.: Secondary organic aerosol formation in cloud droplets and aqueous particles (aqSOA): a review of laboratory, field and model studies, Atmos. Chem. Phys., 11, 11069-11102, https://doi.org/10.5194/acp-11-11069-2011, 2011.

Fang, T., Verma, V., Bates, J. T., Abrams, J., Klein, M., Strickland, M. J., Sarnat, S. E., Chang, H. H., Mulholland, J. A., Tolbert, P. E., Russell, A. G., and Weber, R. J.: Oxidative potential of ambient water-soluble $PM_{2.5}$ in the southeastern United States: contrasts in sources and health associations between ascorbic acid (AA) and dithiothreitol (DTT) assays, Atmos. Chem. Phys., 16, 3865-3879, https://doi.org/10.5194/acp-16-3865-2016, 2016.

Faust, J. A., Wong, J. P., Lee, A. K., and Abbatt, J. P.: Role of aerosol liquid water in secondary organic aerosol formation from volatile organic compounds, Environ. Sci. Technol., 51, 1405-1413, https://doi.org/10.1021/acs.est.6b04700, 2017.

George, K. M., Ruthenburg, T. C., Smith, J., Yu, L., Zhang, Q., Anastasio, C., and Dillner, A. M.: FT-IR quantification of the carbonyl functional group in aqueous-phase secondary organic aerosol from

830   phenols, Atmos. Environ., 100, 230-237, https://doi.org/10.1016/j.atmosenv.2014.11.011, 2015.

831   Gilardoni, S., Massoli, P., Paglione, M., Giulianelli, L., Carbone, C., Rinaldi, M., Decesari, S., Sandrini,

832   S., Costabile, F., Gobbi, G. P., Pietrogrande, M. C., Visentin, M., Scotto, F., Fuzzi, S., and

833   Facchini, M. C.: Direct observation of aqueous secondary organic aerosol from biomass-

834   burning   emissions,   Proc.   Natl.   Acad.   Sci.   USA.,   113,   10013-8,

835   https://doi.org/10.1073/pnas.1602212113, 2016.

836   Gligorovski, S., Strekowski, R., Barbati, S., and Vinoe, D.: Environmental implications of hydroxyl

837   radicals (OH), Chem. Rev., 115(24), 13051-13092, https://doi.org/10.1021/cr500310b, 2015.

838   Guo, Y., Zhang, Y., Yu, G., and Wang, Y., Revisiting the role of reactive oxygen species for pollutant

839   abatement during catalytic ozonation: the probe approach versus the scavenger approach, Appl.

840   Catal. B Environ., 280, 119418, https://doi.org/10.1016/j.apcatb.2020.119418, 2021.

841   He, L., Schaefer, T., Otto, T., Kroflic, A., and Herrmann, H.: Kinetic and theoretical study of the

842   atmospheric aqueous-phase reactions of OH radicals with methoxyphenolic compounds, J. Phys.

843   Chem. A, 123, 7828-7838, https://doi.org/10.1021/acs.jpca.9b05696, 2019.

844   Herrmann, H.: Kinetics of aqueous phase reaction relevant for atmospheric chemistry, Chem. Rev., 103,

845   4691-4716, https://doi.org/10.1021/cr020658q, 2003.

846   Hong, J., Han, B., Yuan, N., and Gu, J.: The roles of active species in photo-decomposition of organic

847   compounds by microwave powered electrodeless discharge lamps, J. Environ. Sci. (China), 33,

848   60-8, https://doi.org/10.1016/j.jes.2014.12.016, 2015.

849   Huang, D., Zhang, X., Chen, Z. M., Zhao, Y., and Shen, X. L.: The kinetics and mechanism of an aqueous

850   phase isoprene reaction with hydroxyl radical, Atmos. Chem. Phys., 11, 7399-7415,

851   https://doi.org/10.5194/acp-11-7399-2011, 2011.

852   Huang, D., Zhang, Q., Cheung, H. H. Y., Yu, L., Zhou, S., Anastasio, C., Smith, J. D., and Chan, C. K.:

853   Formation and evolution of aqSOA from aqueous-phase reactions of phenolic carbonyls:

854   comparison between ammonium sulfate and ammonium nitrate solutions, Environ. Sci.

855   Technol., 52, 9215-9224, https://doi.org/10.1021/acs.est.8b03441, 2018.

856   Jiang, W., Misovich, M. V., Hettiyadura, A. P. S., Laskin, A., McFall, A. S., Anastasio, C., and Zhang, Q.:

857   Photosensitized reactions of a phenolic carbonyl from wood combustion in the aqueous phase-

858   chemical evolution and light absorption properties of aqSOA, Environ. Sci. Technol., 55, 5199-

859   5211, https://doi.org/10.1021/acs.est.0c07581, 2021.

860 Kaur, R., and Anastasio, C.: First measurements of organic triplet excited states in atmospheric waters,

861   Environ. Sci. Technol., 52, 5218-5226, https://doi.org/10.1021/acs.est.7b06699, 2018.

862 Kaur, R., Labins, J. R., Helbock, S. S., Jiang, W., Bein, K. J., Zhang, Q., and Anastasio, C.: Photooxidants

863   from brown carbon and other chromophores in illuminated particle extracts, Atmos. Chem.

864   Phys., 19, 6579-6594, https://doi.org/10.5194/acp-19-6579-2019, 2019.

865 Kroll, J. H., Donahue, N. M., Jimenez, J. L., Kessler, S. H., Canagaratna, M. R., Wilson, K. R., Altieri,

866   K. E., Mazzoleni, L. R., Wozniak, A. S., Bluhm, H., Mysak, E. R., Smith, J. D., Kolb, C. E., and

867   Worsnop, D. R.: Carbon oxidation state as a metric for describing the chemistry of atmospheric

868   organic aerosol, Nat. Chem., 3, 133-9, https://doi.org/10.1038/nchem.948, 2011.

869 Laurentiis, E. D., Socorro, J., Vione, D., Quivet, E., Brigante, M., Mailhot, G., Wortham, H., and

870   Gligorovski, S.: Phototransformation of 4-phenoxyphenol sensitised by 4-

871   carboxybenzophenone: evidence of new photochemical pathways in the bulk aqueous phase and

872   on the surface of aerosol deliquescent particles, Atmos. Environ., 8, 569-578,

873   https://doi.org/10.1016/j.atmosenv.2013.09.036, 2013.

874 Lee, A. K. Y., Hayden, K. L., Herckes, P., Leaitch, W. R., Liggio, J., Macdonald, A. M., and Abbatt, J. P.

875   D.: Characterization of aerosol and cloud water at a mountain site during WACS 2010:

876   secondary organic aerosol formation through oxidative cloud processing, Atmos. Chem. Phys.,

877   12, 7103-7116, https://doi.org/10.5194/acp-12-7103-2012, 2012.

878 Li, F., Tsona, N. T., Li, J., and Du, L.: Aqueous-phase oxidation of syringic acid emitted from biomass

879   burning: formation of light-absorbing compounds, Sci. Total Environ., 765, 144239,

880   https://doi.org/10.1016/j.scitotenv.2020.144239, 2021.

881 Li, Y. J., Huang, D. D., Cheung, H. Y., Lee, A. K. Y., and Chan, C. K.: Aqueous-phase photochemical

882   oxidation and direct photolysis of vanillin-a model compound of methoxy phenols from biomass

883   burning, Atmos. Chem. Phys., 14, 2871-2885, https://doi.org/10.5194/acp-14-2871-2014, 2014.

884 Lim, Y. B., Tan, Y., Perri, M. J., Seitzinger, S. P., and Turpin, B. J.: Aqueous chemistry and its role in

885   secondary organic aerosol (SOA) formation, Atmos. Chem. Phys., 10, 10521-10539,

886   https://doi.org/10.5194/acpd-10-14161-2010, 2010.

887 Lin, M., and Yu, J. Z.: Dithiothreitol (DTT) concentration effect and its implications on the applicability

888   of DTT assay to evaluate the oxidative potential of atmospheric aerosol samples, Environ.

889   Pollut., 251, 938-944, https://doi.org/10.1016/j.envpol.2019.05.074, 2019.

Mabato, B. R. G., Lyu, Y., Ji, Y., Li, Y., Huang, D., Li, X., Nah, T., Lam, C. H., and Chan, C. K.: Aqueous secondary organic aerosol formation from the direct photosensitized oxidation of vanillin in the absence and presence of ammonium nitrate, Atmos. Chem. Phys., 22, 273-293, https://doi.org/10.5194/acp-22-273-2022, 2022.

McWhinney, R. D., Zhou, S., and Abbatt, J. P. D.: Naphthalene SOA: redox activity and naphthoquinone gas–particle partitioning, Atmos. Chem. Phys., 13, 9731-9744, https://doi.org/10.5194/acp-13-9731-2013, 2013.

Mladenov, N, Alados-Arboledas, L., Olmo, F .J., Lyamani, H., Delgado, A., Molina, A., and Reche, I.: Applications of optical spectroscopy and stable isotope analyses to organic aerosol source discrimination in an urban area, Atmos. Environ., 45, 1960-1969, https://doi.org/ 10.1016/j.atmosenv.2011.01.029, 2011.

Nau, W. M., and Scaiano, J. C.: Oxygen quenching of excited aliphatic ketones and diketones, J. Phys. Chem., 100, 11360-11367, https://doi.org/10.1021/jp960932i, 1996.

Ng, N. L., Canagaratna, M. R., Zhang, Q., Jimenez, J. L., Tian, J., Ulbrich, I. M., Kroll, J. H., Docherty, K. S., Chhabra, P. S., Bahreini, R., Murphy, S. M., Seinfeld, J. H., Hildebrandt, L., Donahue, N. M., DeCarlo, P. F., Lanz, V. A., Prevot, A. S. H., Dinar, E., Rudich, Y., and Worsnop, D. R.: Organic aerosol components observed in Northern Hemispheric datasets from aerosol mass spectrometry, Atmos. Chem. Phys., 10, 4625-4641, https://doi.org/10.5194/acp-10-4625-2010, 2010.

Pan, Y., Ma, H., Li, Z., Du, Y., Liu, Y., Yang, J., and Li, G.: Selective conversion of lignin model veratryl alcohol by photosynthetic pigment via photo-generated reactive oxygen species, Chem. Eng. J, 393, 124772, https://doi.org/10.1016/j.cej.2020.124772, 2020.

Raja, P., Bozzi, A., Mansilla, H., and Kiwi, J.: Evidence for superoxide-radical anion, singlet oxygen and OH-radical intervention during the degradation of the lignin model compound (3-methoxy-4-hydroxyphenylmethylcarbinol), J. Photochem. Photobiol. Chem., 169, 271-278, https://doi.org/10.1016/j.jphotochem.2004.07.009, 2005.

Rossignol, S., Aregahegn, K. Z., Tinel, L., Fine, L., Nozière, B., and George, C.: Glyoxal induced atmospheric photosensitized chemistry leading to organic aerosol growth, Environ. Sci. Technol., 48, 3218-3227, https://doi.org/10.1021/es405581g, 2014.

Scharko, N. K., Berke, A. E., and Raff, J. D.: Release of nitrous acid and nitrogen dioxide from nitrate

920   photolysis in acidic aqueous solutions, Environ. Sci. Technol., 48, 11991-2001,

921   https://doi.org/10.1021/es503088x, 2014.

922   Smith, J. D., Kinney, H., and Anastasio, C.: Aqueous benzene-diols react with an organic triplet excited

923   state and hydroxyl radical to form secondary organic aerosol. Phys. Chem. Chem. Phys., 17,

924   10227, https://doi.10.1039/c4cp06095d, 2015.

925   Smith, J. D., Sio, V., Yu, L., Zhang, Q., and Anastasio, C.: Secondary organic aerosol production from

926   aqueous reactions of atmospheric phenols with an organic triplet excited state, Environ. Sci.

927   Technol., 48, 1049-1057, https://doi.org/10.1021/es4045715, 2014.

928   Sun, Y., Zhang, Q., Anastasio, C., and Sun, J.: Insights into secondary organic aerosol formed via

929   aqueous-phase reactions of phenolic compounds based on high resolution mass spectrometry,

930   Atmos. Chem. Phys., 10, 4809–4822, https://doi.org/10.5194/acp-10-4809-2010, 2010.

931   Tang, S., Li, F., Tsona, N.T., Lu, C., Wang, X., and Du, L.: Aqueous-phase photooxidation of vanillic

932   acid: a potential source of humic-like substances (HULIS), ACS Earth Space Chem., 4, 862-

933   872, https://doi.org/10.1021/acsearthspacechem.0c00070, 2020.

934   Verma, V., Fang, T., Xu, L., Peltier, R. E., Russell, A. G., Ng, N. L., and Weber, R. J.: Organic aerosols

935   associated with the generation of reactive oxygen species (ROS) by water-soluble $PM_{2.5}$,

936   Environ. Sci. Technol., 49, 4646-56, https://doi.org/10.1021/es505577w, 2015a.

937   Verma, V., Wang, Y., El-Afifi, R., Fang, T., Rowland, J., Russell, A.G., and Weber, R. J.: Fractionating

938   ambient humic-like substances (HULIS) for their reactive oxygen species activity-assessing the

939   importance of quinones and atmospheric aging, Atmos. Environ., 120, 351-359,

940   https://doi.org/10.1016/j.atmosenv.2015.09.010, 2015b.

941   Vione, D., Albinet, A., Barsotti, F., Mekic, M., Jiang, B., Minero, C., Brigante, M., and Gligorovski, S.:

942   Formation of substances with humic-like fluorescence properties, upon photoinduced

943   oligomerization of typical phenolic compounds emitted by biomass burning, Atmos. Environ.,

944   206, 197-207, https://doi.org/10.1016/j.atmosenv.2019.03.005, 2019.

945   Vione, D., Maurino, V., Minero, C., Pelizzetti, E., Harrison, M. A., Olariu, R. I., and Arsene, C.:

946   Photochemical reactions in the tropospheric aqueous phase and on particulate matter, Chem.

947   Soc. Rev., 35, 441-53, https://doi.org/10.1039/b510796m, 2006.

948   Vione, D., Maurino, V., and Minero, C.: Photosensitised humic-like substances (HULIS) formation

949   processes of atmospheric significance: a review, Environ. Sci. Pollut. Res., 21, 11614-11622,

950	https://doi.org/10.1007/s11356-013-2319-0, 2014.

951	Wang, L., Lan, X., Peng, W., and Wang, Z.: Uncertainty and misinterpretation over identification,

952	quantification and transformation of reactive species generated in catalytic oxidation processes:

953	A review, J Hazard. Mater., 408, 124436, https://doi.org/10.1016/j.jhazmat.2020.124436, 2021.

954	Wu, G., Ram, K., Fu, P., Wang, W., Zhang, Y., Liu, X., Stone, E. A., Pradhan, B. B., Dangol, P. M.,

955	Panday, A., Wan, X., Bai, Z., Kang, S., Zhang, Q., and Cong, Z.: Water-soluble brown carbon

956	in atmospheric aerosols from Godavari (Nepal), a regional representative of south Asia, Environ.

957	Sci. Technol., 53, 3471-3479, https://doi.org/10.1021/acs.est.9b00596, 2019.

958	Xie, M., Mladenov, N., Williams, M. W., Neff, J. C., Wasswa, J., and Hannigan, M. P.: Water soluble

959	organic aerosols in the Colorado Rocky Mountains, USA: composition, sources and optical

960	properties, Sci. Rep., 6, https://doi.org/10.1038/srep39339, 2016.

961	Yang, J., Au, W. C., Law, H., Lam, C. H., and Nah, T.: Formation and evolution of brown carbon during

962	aqueous-phase nitrate-mediated photooxidation of guaiacol and 5-nitroguaiacol, Atmos.

963	Environ., 254, 118401, https://doi.org/10.1016/j.atmosenv.2021.118401, 2021.

964	Ye, Z., Zhuang, Y., Chen, Y., Zhao, Z., Ma, S., Huang, H., Chen, Y., and Ge, X.: Aqueous-phase oxidation

965	of three phenolic compounds by hydroxyl radical: Insight into secondary organic aerosol

966	formation yields, mechanisms, products and optical properties, Atmos. Environ., 223, 117240,

967	https://doi.org/10.1016/j.atmosenv.2019.117240, 2020.

968	Yu, L., Smith, J., Laskin, A., Anastasio, C., Laskin, J., and Zhang, Q.: Chemical characterization of SOA

969	formed from aqueous-phase reactions of phenols with the triplet excited state of carbonyl and

970	hydroxyl radical, Atmos. Chem. Phys., 14, 13801–13816, https://doi.org/10.5194/acp-14-

971	13801-2014, 2014.

972	Yu, L., Smith, J., Laskin, A., George, K. M., Anastasio, C., Laskin, J., Dillner, A. M., and Zhang, Q.:

973	Molecular transformations of phenolic SOA during photochemical aging in the aqueous phase:

974	competition among oligomerization, functionalization, and fragmentation, Atmos. Chem. Phys.,

975	16, 4511-4527, https://doi.org/10.5194/acp-16-4511-2016, 2016.

976	Zhang, X., Chen, Z. M., and Zhao, Y.: Laboratory simulation for the aqueous OH-oxidation of methyl

977	vinyl ketone and methacrolein: significance to the in-cloud SOA production, Atmos. Chem.

978	Phys., 10, 9551-9561, https://doi.org/10.5194/acp-10-9551-2010, 2010.

979	Zhao, R., Lee, A. K., and Abbatt, J. P.: Investigation of aqueous-phase photooxidation of glyoxal and

980   methylglyoxal by aerosol chemical ionization mass spectrometry: observation of

981   hydroxyhydroperoxide   formation,   J.   Phys.   Chem.   A.,   116,   6253-63,

982   https://doi.org/10.1021/jp211528d, 2012.

983 Zhao, R., Mungall, E. L., Lee, A. K. Y., Aljawhary, D., and Abbatt, J. P. D.: Aqueous-phase

984   photooxidation of levoglucosan-a mechanistic study using aerosol time of flight chemical ionization

985   mass   spectrometry   (Aerosol   ToF-CIMS),   Atmos.   Chem.   Phys.,   14,   9695-9706,

986   https://doi.org/10.5194/acpd-14-8819-2014, 2014.

987 Zhou, Z., Chen, B., Qu, X., Fu, H., and Zhu, D.: Dissolved black carbon as an efficient sensitizer in the

988   photochemical transformation of 17#-estradiol in aqueous solution, Environ. Sci. Technol., 52,

989   10391-10399, https://doi.org/10.1021/acs.est.8b01928, 2018.